Non-Newtonian Patient-specific Simulations of Left Atrial Hemodynamics

*A. Gonzalo[a,b], M. García-Villalba[c], L. Rossini[a], E. Durán[c], D. Vigneault[d], P. Martínez-Legazpi[e,f], O. Flores[c], J. Bermejo[e,f,g,h], E. McVeigh[d,i], A. M. Kahn[j], and J. C. del Alamo[a,b,k,l]

[a] *Dept. of Mechanical and Aerospace Eng., University of California San Diego, La Jolla, CA, United States*

[b] *Dept. of Mechanical Eng., University of Washington, Seattle, WA, United States*

[c] *Dept. Bioingeniería e Ing. Aeroespacial, Universidad Carlos III de Madrid, 28911 Leganés, Spain*

[d] *Dept. of Bioengineering, University of California San Diego, La Jolla, CA, United States*

[e] *Hospital General Universitario Gregorio Marañón, Madrid, Spain*

[f] *Instituto de Investigación Sanitaria Gregorio Marañón, Madrid, Spain*

[g] *Facultad de Medicina, Universidad Complutense de Madrid, Madrid, Spain*

[h] *CIBERCV, Madrid, Spain*

[i] *Dept. of Radiology, University of California San Diego, La Jolla, CA, United States*

[j] *Division of Cardiovascular Medicine, University of California San Diego, La Jolla, CA, United States*

[k] *Center for Cardiovascular Biology, University of Washington, Seattle, WA, United States*

[l] *Institute for Stem Cell and Regenerative Medicine, University of Washington, Seattle, WA, United States*

Abstract

Atrial fibrillation (AF) is the most common arrhythmia, affecting $\sim$ 35M people worldwide. The irregular beating of the left atrial (LA) caused by AF impacts the LA hemodynamics increasing the risk of thrombosis and ischemic stroke. Most LA thrombi appear in its appendage (LAA), a narrow sac of varied morphology where blood is prone to stagnate. In the LAA, the combination of slow blood flow and low shear rates $\left(< 100\ \mathrm{s}^{-1}\right)$ promotes the formation of red blood cell aggregations called rouleaux. Blood experiences a non-Newtonian behavior when rouleaux formed that has not been considered in previous CFD analysis of the LA. We model the anatomy and motion of the LA from 4D-CT images and solve the blood flow inside the LA geometry with our CFD in-house code, which models Non-Newtonian rheology with the shear-hematocrit-dependent Carreau-Yasuda equation. We cover a wide range of non-Newtonian effects considering a small and a large hematocrit, including an additional constitutive relation to account for the rouleaux formation time, and we compare our results with Newtonian simulations. Blood rheology influence in LAA hemostasis is studied in 6 patient-specific anatomies. Two subjects had an LAA thrombus (digitally removed before running the simulations), another had a history of TIAs, and the remaining three had normal atrial function. In our simulations, the shear rate remains below 50 s^{-1} in the LAA for all non-Newtonian models considered. This triggers an increase of viscosity that alters the flow behavior in that site, which exhibits different flow patterns than Newtonian simulations. These hemodynamic changes translate into differences in the LAA hemostasis, calculated with the residence time. This metric accumulates over several cycles experiencing an increase in its maximum and averaged values in the LAA when non-Newtonian blood rheology is considered, especially for high hematocrit levels. Overall, our analysis suggests that non-Newtonian effects should not be neglected in patient-specific CFD LA simulations since they have an important impact on the predicted values of LAA residence time.

1 Introduction

Cardiac thrombo-embolism leading to ischemic stroke is a leading cause of mortality and disability. Ischemic strokes account for two thirds of all strokes, which are estimated to be 26 million per year worldwide [1]. Approximately 30% of these ischemic strokes are directly associated with atrial fibrillation (AF), a common arrhythmia affecting 35 million people worldwide [2]. Notably, these embolic strokes are associated with worse outcomes than ischemic strokes in the absence of AF [3]. An additional 30% of ischemic strokes are categorized as embolic strokes from undetermined source (ESUS), and increasing evidence suggests many of these also have a cardioembolic origin [4]. Specifically, a significant fraction of these ESUS are linked to left atrial thrombosis, both in the presence of subclinical AF and in sinus rhythm [5, 6]. Anticoagulation therapy can help prevent cardioembolic stroke, but this therapy increases the risk of internal hemorrhages. Therefore, anticoagulant drugs are prescribed only to patients whose stroke risk overweighs the bleeding risk. In patients with AF, clinical tools to estimate stroke risk are based on demographic and comorbid factors (*e.g.*, the CHA2DS2-VASc score), which cannot capture patient-specific thrombogenesis mechanisms and have a modest predictive accuracy [7]. Likewise, indiscriminate anticoagulation of ESUS patients has not proven effective in preventing recurrent strokes despite increasing bleeding event rates [8]. In summary, left atrial thrombosis is a major source of ischemic strokes, and there is a pressing need for predictive quantification of this process in patient-specific models.

Thrombogenesis requires the concurrence of three phenomena: endothelial damage or dysfunction, the presence of procoagulatory factors in the blood, and increased blood stasis [9]. In the left atrium (LA), most thrombi form inside the left atrial appendage (LAA), a narrow hooked sac that accounts for approximately 5-10% of LA volume and varies greatly in morphology among individuals [10]. The Irregular or weak beating of the heart together with anatomical factors promote the appearance of LAA stasis [11, 12]. Intracavitary blood stasis and thrombogenesis risk can be quantified through blood residence time, *i.e.*, the time span spent by blood particles inside a cardiac chamber [13]. Progress in computational fluid dynamics (CFD) algorithms and computer processing capacity now make it feasible to simulate blood flow in four-chamber domains [14], two-chamber domains (typically the left heart) [15, 16, 17], and single-chamber domains (typically the left ventricle) [18, 19, 20, 21, 22, 23, 24, 25]. Some of these simulations include models of heart valve motion [22, 26, 15, 17, 27, 28, 29] and some can resolve the intricate domain surface caused by endocardial trabeculation [28, 29]. Motivated by the need for patient-specific prediction of LAA blood stasis, the number of CFD simulations of LA flow is proliferating [30, 31, 32, 33, 34, 35].

Blood inside the cardiac chambers is usually modeled as a Newtonian fluid based on the assumption that its shear rate is high enough to prevent the formation of red blood cell (RBC) aggregates and that, even if some low-shear pockets may occasionally form, their lifetime is shorter than the RBC aggregation timescale [36, 37]. While an exhaustive validation of these modeling assumptions can be challenging, Newtonian CFD simulations provide intracardiac flow velocity fields that agree reasonably well with phase-contrast MRI data from the same patients [21, 38]. Nevertheless, calculating residence time inside the LAA has two peculiarities that make it particularly sensitive to non-Newtonian effects. First, high-resolution CFD data has shown that both low shear rate and high residence time coexist inside the LAA [33, 35], making this site prone to RBC aggregation. Consonantly, spontaneous echocardiographic contrast or "smoke", which is caused by red blood cell aggregates under low shear [39], is frequently observed in the LAA by transesophageal echocardiography and is associated with blood stasis [40]. Second, in contrast to flow metrics like kinetic energy, wall shear stress, or oscillatory shear index, residence time is cumulatively integrated over multiple heartbeats. Therefore, slight differences in instantaneous velocity could gradually accumulate to generate appreciable differences in residence time. Considering that blood is a shear-thinning fluid, Newtonian CFD analysis could underestimate blood stasis, and this effect could be more severe for regions of significant stasis.

The present study evaluates whether blood's shear-thinning rheology significantly affects CFD estimations of LAA blood stasis. To this end, we carried out numerical simulations of left atrial flow considering a Carreau-Yasuda constitutive relation, and compared the results with those from Newtonian simulations [35]. We examined $N = 6$ patients covering a wide range of atrial morphology and function, three of whom had LAA thrombosis or a history of transient ischemic attacks (TIAs). Our results indicate that blood stasis increases in low-shear regions when non-Newtonian rheology is considered, especially in the LAA. This trend is robust for different constitutive laws that consider the timescale of RBC aggregation and a wide range of hematocrit (hct) levels.

2 Methods

2.1 Patient population, image acquisition, image reconstruction, and mesh generation

We retrospectively considered the $N = 6$ left atrial models of García-Villalba *et al.* [35], consisting of 4D (3D, time-resolved) patient-specific segmentations of human left atria obtained from computed tomography (CT) imaging. Three patients had normal LA volume and function, were imaged in sinus rhythm, and did not have a left atrial appendage (LAA) thrombus. The other three patients were imaged in atrial fibrillation (AF), had an enlarged LA chamber, and impaired LA global function. Two of these had an LAA thrombus (removed digitally before running the simulations), and one had a history of transient brain ischemic attacks (TIAs). Cardiac-gated cine CT scans were performed following standard clinical protocols at each participating center (NIH, Bethesda, MD and UCSD, La Jolla, CA). The images were reconstructed using the CT scanner manufacturers' standard algorithms, yielding DICOM files with resolutions between 0.32 mm and 0.48 mm in the x-y axial plane and 0.5 mm to 1 mm in the z-direction. Time-resolved images were obtained at regularly spaced time points across the cardiac cycle, ranging between 5% and 10% of the R-R interval.

The computational LA meshes were generated in four steps using itk-SNAP [41] and MATLAB. The first step consisted of segmenting the 3D LA anatomy in each time frame of the 4D CT image sequence, and identifying the PV inlets, mitral annulus, and LAA. For each 3D segmentation, a triangular surface mesh was created and then resampled to match the computational fluid dynamics (CFD) solver's resolution [42]. The resulting triangular meshes were registered across the cardiac cycle and their positions yielding a coherent triangle vertex and centroid cloud [43]. Finally, the positions of these points were expressed as a Fourier temporal series to provide interpolated boundary conditions to the CFD solver at time points not contained in the 4D CT sequence. Figure 1 and Table 1 summarize the main anatomical and functional features of the patients' atria. For more detailed information on patient selection, imaging acquisition and reconstruction, and mesh generation, the reader is referred to García-Villalba *et al.* [35].

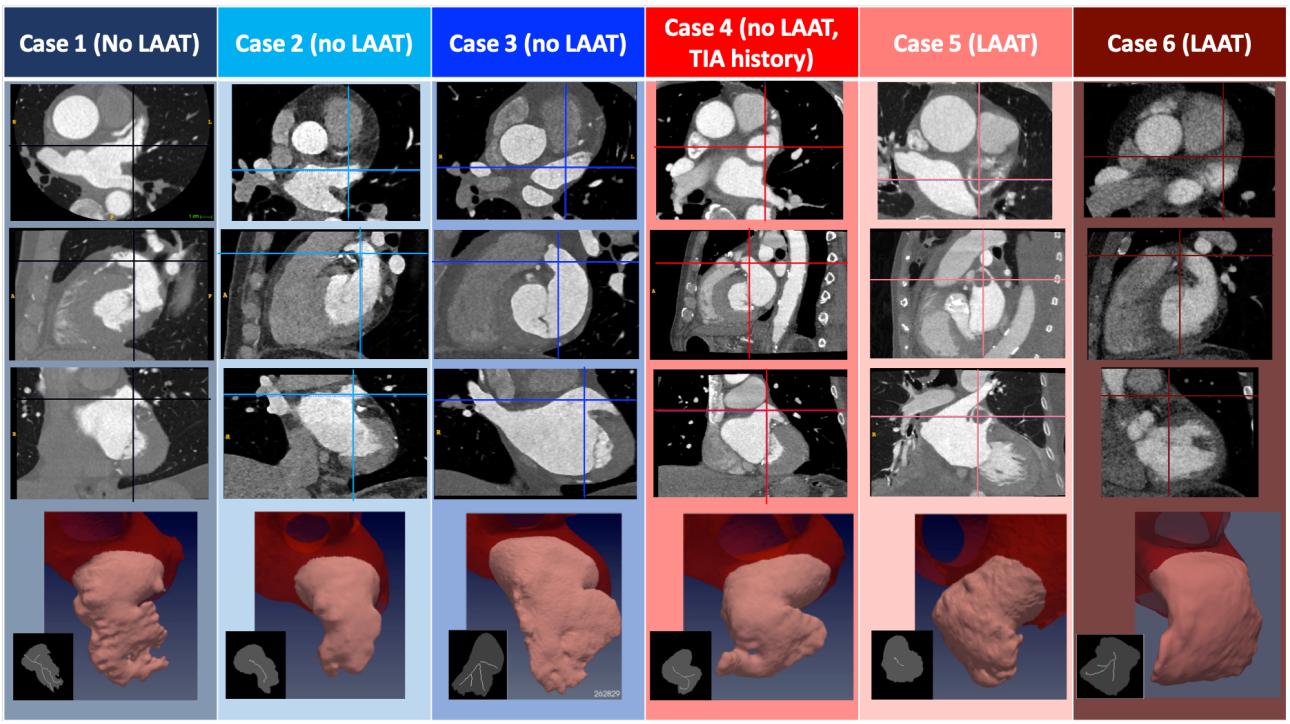

Figure 1: **Anatomical Features of Patient-Specific Subjects.** The three first rows display CT images corresponding to the $N = 6$ subjects studied. The images represent, from top to bottom, axial, sagittal and coronal plane sections showing the left atrium, and including LAA thrombi if present (patients 5 and 6). In each panel, the intersections with the other two view planes are represented with a vertical and a horizontal line. The bottom row displays a 3D rendering of the segmented LAA for each subject, and an inset showing its plane projection (gray) and the branches that define the LAA lobes (white). Data are shown at an instant corresponding to 50% of the R-R interval.

Subject Number	1	2	3	4	5	6
LAA Thrombus (or history of TIA)	No	No	No	TIAs	Yes	Yes
Sinus Rhythm	Yes	Yes	Yes	No	No	No
Mean LA Volume (ml)	86.6	70.1	115	145	157	180
Min. LA Volume (V_{LA}^{min}, ml)	59.6	49.0	87.2	119	150	157
Max. LA Volume (V_{LA}^{max}, ml)	108	91.2	145	155	165	205
Mean LAA Volume (ml)	6.94	4.85	14.3	10.7	15.5	22.0
Min. LAA Volume (V_{LAA}^{min}, ml)	4.32	3.14	10.2	9.10	13.8	19.8
Max. LAA Volume (V_{LAA}^{max}, ml)	8.97	6.28	17.9	11.6	17.4	24.7
Pre-A-wave Volume (V_{LA}^{pre-A}, ml)	94.3	72.3	119	149	153	178
LA Sphericity	0.80	0.82	0.78	0.86	0.83	0.81
Global (LA EF) $\left[\frac{V_{LA}^{max}-V_{LA}^{min}}{V_{LA}^{max}}\right]$	0.45	0.46	0.40	0.23	0.091	0.23
LAA EF $\left[\frac{V_{LAA}^{max}-V_{LAA}^{min}}{V_{LAA}^{max}}\right]$	0.52	0.50	0.43	0.22	0.21	0.20
Expansion Index $\left[\frac{V_{LA}^{max}-V_{LA}^{min}}{V_{LA}^{min}}\right]$	0.81	0.86	0.66	0.30	0.10	0.31
Passive EF $\left[\frac{V_{LA}^{max}-V_{LA}^{pre-A}}{V_{LA}^{max}}\right]$	0.13	0.21	0.18	0.039	0.073	0.13
Booster EF $\left[\frac{V_{LA}^{pre-A}-V_{LA}^{min}}{V_{LA}^{pre-A}}\right]$	0.37	0.32	0.27	0.20	0.020	0.12
$\frac{\textbf{Conduit Volume}}{\textbf{LV Stroke Volume}}$ $\left[1-\frac{V_{LA}^{max}-V_{LA}^{min}}{SV}\right]$	0.33	0.50	0.41	0.46	0.80	0.63
PVs (ml)	43	38	51	36	17	49
PVd (ml)	65	58	60	52	63	94
PVs-PVd ratio	0.66	0.66	0.84	0.69	0.27	0.52
PVa (ml)	17	7.3	12	13	0.14	1.4
PVa duration (cycles)	0.11	0.11	0.13	0.12	0.039	0.068
A-wave duration (cycles)	0.22	0.25	0.30	0.18	0.21	0.23
PVa − A wave duration ratio	0.49	0.43	0.44	0.64	0.18	0.30
E/A ratio	1.64	2.36	3.03	2.05	3.86	3.65

Table 1: **Summary of anatomical and functional parameters of the left atrium (LA) and its appendage (LAA) in the LAAT/TIA-neg (left three columns) and LAAT/TIAA-pos (right three columns) groups.** Mean volume indicates time-averaged volume. EF, ejection fraction; PVs, blood volume that enters the LA during LV systole; PVd, blood volume that enters the LA during LV diastole; PVa, blood volume that exits the LA due to reverse flow volume through the pulmonary veins during atrial contraction; E/A ratio, ratio of peak mitral velocities during early diastole (E-wave) and atrial contraction (A-wave).

2.2 Computational Fluid Dynamic

Flow simulations were performed using a modified version of the in-house CFD code TUCAN [44, 45], which we had previously adapted to simulate incompressible, Newtonian flow in the left atrium [35, 46]. To account for non-Newtonian effects, we consider the Navier-Stokes equations

$$\frac{\partial \overrightarrow{u}}{\partial t} + \left(\overrightarrow{u} \cdot \nabla\right) \overrightarrow{u} = -\frac{1}{\rho} \nabla p + \nabla \cdot \bar{\bar{\tau}}, \tag{1}$$

where $\overrightarrow{u}$ and p are respectively the velocity and pressure fields, ρ is the fluid density, and τ is the stress tensor. The stress tensor is defined as $\bar{\bar{\tau}} = 2\nu\left(S\right)\bar{\bar{\epsilon}}$, where ν is the fluid kinematic viscosity, $\bar{\bar{\epsilon}} = \left(\nabla \overrightarrow{u} + \nabla \overrightarrow{u}^T\right)/2$ is the rate of strain tensor, $S = 2\sqrt{|\epsilon_2|}$ is the shear rate, and ϵ_2 the the second invariant of $\bar{\bar{\epsilon}}$. The constitutive relation between ν and S is based on the Carreau-Yasuda model [47], both in its original form and with modifications to account for blood's thixotropic behavior under unsteady flow. Section 2.3 below provides more details about the constitutive models implemented in our CFD code.

The Navier-Stokes equations were integrated in time by a low-storage, three-stage, semi-implicit Runge–Kutta scheme using a fractional-step method. The constitutive law was treated semi-implicitly by splitting the kinematic viscosity coefficient into two terms, *i.e.*, $\nu\left(S\right) = \nu_{imp} + \Delta\nu_{exp}\left(S\right)$, where ν_{imp} is a constant coefficient. Consonantly, the viscous stresses were split as $\nabla \cdot \bar{\bar{\tau}} = \nu_{imp}\nabla^2 \overrightarrow{u} + \nabla \cdot \left[\Delta\nu_{exp}\left(S\right)\left(\nabla \overrightarrow{u} + \nabla \overrightarrow{u}^T\right)\right]$; the first, linear term was integrated in time implicitly, whereas the second, non-linear term was integrated explicitly. We chose $\nu_{imp} = \nu_\infty$ but note that the implementation is independent of this particular choice, offering

some control over the stability of the temporal integration. The time step Δt of each simulation was constant and set to keep the Courant-Friedrichs-Lewy (CFL) number below 0.2 across the whole simulation. To account for the additional non-linear terms originating from $\Delta\nu_{exp}(S)$, the Courant number was re-defined as $CFL_{mod} = [|\overrightarrow{u}| + |\nabla(\Delta\nu_{exp})|]\,\Delta t/\Delta x = CFL + |\nabla(\Delta\nu_{exp})|\,\Delta t/\Delta x$. The spatial discretization was performed on a staggered Cartesian grid with a centered, second-order, finite difference scheme. The grid spacing, $\Delta x = 0.51$ mm $\left(256^3 \text{ grid points}\right)$, was isotropic and uniform. We initialized each non-Newtonian simulation using the velocity field previously calculated with Newtonian rheology in the same LA mesh [35]. Then, the simulations were ran for 15 heartbeats in a grid of relatively coarse-resolution $\left(\Delta x_c = 16\Delta x/9,\ 144^3 \text{ grid points}\right)$ to let the flow transition from Newtonian to non-Newtonian. Finally, we interpolated the flow variables into the 256^3 nominal grid and ran the simulations for 6 more heartbeats.

The time spent by blood particles inside the LA chamber was denoted residence time, T_R, and calculated together with the velocity field by solving the forced transport equation [48]

$$\frac{\partial T_R}{\partial t} + \nabla \cdot (\overrightarrow{u} T_R) = 1. \tag{2}$$

This equation was integrated in time explicitly with a low-storage, three-stage Runge-Kutta scheme. Its spatial discretization third-order WENO scheme to balance accuracy with preventing spurious oscillations caused by the Gibbs phenomenon in regions with sharp gradients [49]. Together with the shear rate, the residence time is used as an indicator of blood stasis and non-Newtonian rheology.

The flow was driven by the heart's wall motion obtained from patient-specific 4D CT images, which was imposed using the immersed boundary method (IBM) as previously described [35, 50]. In short, the segmented LA surface was placed inside a 13 cm cubic Cartesian mesh, and free-slip boundary conditions were imposed at the mesh boundaries. No-slip boundary conditions were imposed at the LA surface by adding an appropriate volumetric force term to the Navier-Stokes equations. To enforce flow rates through these pulmonary vein (PV) inlets, a buffer region was defined upstream of each PV inlet plane and the IBM was applied in this region to bring the flow velocity to the desired value. A similar procedure was used to set T_R equal to zero at the PV inlets. No additional boundary conditions are needed for the T_R equation, which only contains first-order derivatives.

The flow velocity through each PV inlet was $\overrightarrow{v}_i = \frac{Q_i}{A_i}\overrightarrow{n}$, where Q_i, A_i and $\overrightarrow{n}$ are the flow rate, inlet area, and normal vector ($i = 1 \ldots 4$). The Q_i's were determined from mass conservation as $Q_i = \frac{1}{4}\left(\frac{dV_{LA}}{dt} - \frac{dV_{LV}}{dt}\right)$, where V_{LA} and V_{LV} are the time-dependent left atrial and left ventricular volumes obtained from each patient's 4D CT scan. This ¼ factor evenly splits the total flow rate through the four PVs. We note that, while it is possible to derive a 0D model of the pulmonary circulation to determine each PV's split of the total PV flow rate, fixing the value of the model impedances would be equivalent to directly specifying the flow split. The actual flow split is patient-specific and, given that the right lung has one more lobe than the left lung, the right PVs typically discharge more flow into the LA than the left PVs [29]. However, Lantz *et al.* [29] reported that flow velocities from simulations with evenly split PV flow rates agree reasonably well with patient-specific phase contrast MRI data. Furthermore, we conducted simulations for the $N = 6$ subjects considered in this study, finding that LA blood residence time and kinetic energy do not experience significant differences when left/right flow splits of 0.4/0.6 or 0.45/0.55 are considered [51]. Finally, we note that we did not model the geometry or motion of the mitral valve leaflets, based on previous evidence that they do not affect LA hemodynamics [16].

2.3 Non-Newtonian constitutive models

We ran simulations with four constitutive laws. First, we used the original Carreau-Yasuda model

$$\nu(S) = \nu_\infty + (\nu_0 - \nu_\infty)\left(1 + (\lambda S)^a\right)^{\frac{n-1}{a}}, \tag{3}$$

where, λ, $n < 1$, and a are blood hematocrit-dependent parameters, and ν_∞ is the reference Newtonian viscosity corresponding to the limit $S \gg \lambda^{-1}$. In this model, yield-stress is represented by prescribing a large value to the zero-shear-rate viscosity coefficient, ν_0, which we prescribed as $\nu_0 = 16\nu_\infty$ similar to de Vita *et al.* [27].

To investigate the effect of the hematocrit, we considered two different sets of parameter values derived from the literature, namely $\lambda = 8.2$ s, $a = 0.64$, $n = 0.2128$ from Leuprecht and Perktold [52], and $\lambda = 3.313$ s, $a = 2$, $n = 0.3568$ from Al-Azawy *et al.* [53]. Although these studies considered $\nu_\infty = 0.035$ cm/s^2, we chose $\nu_\infty = 0.04$ cm/s^2 to facilitate the comparison with our previous Newtonian simulations [35], which where run with a constant kinematic viscosity equal to 0.04 cm/s^2. Figure 2A shows that the shear-rate-dependent kinematic viscosities obtained from the two parameter sets differ significantly. We used the blood rheology

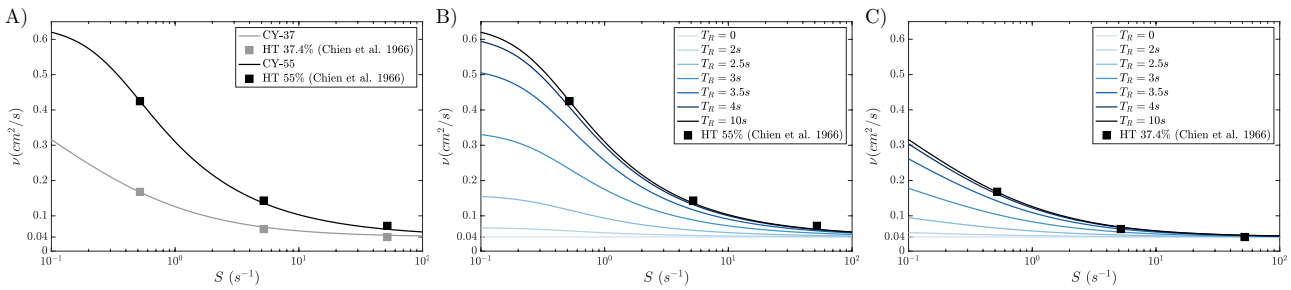

Figure 2: **Non-Newtonian constitutive laws used in the present simulations. A)** Kinematic viscosity $\nu\,(S)$ as a function of shear rate S for the two versions of the Carreau-Yasuda law (eq. 3) used in our simulations. Grey line: CY-37 model with $\lambda = 8.2$ s, $a = 0.64$, $n = 0.2128$, $\nu_0 = 16\nu_\infty$, and $\nu_\infty = 0.04$ cm/s^2; black line: CY-55 model with $\lambda = 3.313$ s, $a = 2$, $n = 0.3568$, $\nu_0 = 16\nu_\infty$, and $\nu_\infty = 0.04$ cm/s^2. The square symbols correspond to datapoints from the empirical law of Chien *et al.* [54] for hematocrit values $Hct = 37.4\%$ (grey) and $Hct = 55\%$ (black). Kinematic viscosity $\nu\,(S, T_R)$ as a function of shear rate S and residence time T_R for the residence-time-activated Carreau-Yasuda models **B)** CY-T_R-55 and **C)** CY-T_R-37 (eqs. 4-5). Black squares come from Chien et al.'s [54] data for the respective *Hct* values.

experiments of Chien *et al.* [54] to estimate their associated *Hct* values, obtaining excellent fits for $Hct = 37.4$ and 55 (Figure 2A). Hence, we refer to these models as CY-37 and CY-55 throughout this manuscript. Blood hematocrit levels can vary significantly with age and sex, with all-age normal ranges (defined as the 2.5-97.5 percentile range) being $[34-36, 48-50]$ for females and $[39-40, 54]$ for males [55, 56]. Thus, the CY-37 and CY-55 models are helpful to estimate the smallest and largest non-Newtonian effects to be expected in LA hemodynamics.

The Carreau-Yasuda constitutive relation assumes microstructural equilibrium but blood is a thixotropic fluid that exhibits time-dependent rheology because the formation and rupture of RBC rouleaux does not occur infinitely fast [47]. While the observation of LA and LAA echocardiographic "smoke" in patients demonstrates that rouleaux do form in these chambers [39, 40], the unsteady nature of atrial hemodynamics calls for evaluating the interplay between fluidic and thixotropic timescales. Huang and Fabisiak [57] modeled the thixotropic behavior of blood using a power-law term restrained by an exponential term that considered the cumulative exposure of RBCs to shear, *i.e.*, proportional to $S^n \exp\left(-T_1^{-1}\int_0^t S^n dt\right)$. In this model, T_1 is the time scale associated to rouleaux formation and breakdown. Parameter fitting to human blood samples in healthy subjects yielded T_1 values ranging between 3.6 and 6.2 seconds. Consonantly, Schmid-Schönbein *et al.* [58] had previously reported the half-time for RBC aggregation in blood to be 3–5 seconds for normal blood samples and 0.5–1.5 seconds for pathologically hypercoagulable samples. More recently, Arzani [37] proposed a modified Carreau-Yasuda constitutive relation where non-Newtonian effects are activated based on the local value of the residence time. In the same spirit, we ran simulations where blood viscosity was given by

$$\nu\,(S, T_R) = \nu_\infty + H\,(T_R)\,(\nu_0 - \nu_\infty)\,(1 + (\lambda S)^a)^{\frac{n-1}{a}}\,, \tag{4}$$

$$H\,(T) = \frac{1 + \mathrm{erf}\left[(T - T_\mu)\,/\,\left(\sqrt{2}\sigma\right)\right]}{2},\ T_\mu = 3\text{ s},\ \sigma = 0.6\text{ s}, \tag{5}$$

which provides a smooth transition from Newtonian to non-Newtonian behavior for residence times comparable to experimentally reported RBC aggregation timescales [58, 57]. We ran simulations at Hct = 37 and 55 with the constitutive model in eqs. (4-5), which we denoted as CY-T_R-37 and CY-T_R-55. Figure 2B illustrates the dependence of the CY-T_R-55 model with residence time, showing that non-Newtonian effects are negligible for $T_R \lesssim 2$ s, gradually increase for 2s $\lesssim T_R \lesssim 10$ s, and become indistinguishable from those of the classic Carreau-Yasuda model for $T_R \gtrsim 10$ s. The dependence of the CY-T_R-37 model with residence time is similar (Figure 2C).

3 Results

3.1 Flow visualization in Newtonian and non-Newtonian left atrial simulations

We first evaluated whether the LA body and LAA's overall flow patterns were affected when non-Newtonian blood rheology was considered. Figure 3 displays 3D maps of blood velocity vectors in one of our normal subjects, computed by the Newtonian simulations as well as the non-Newtonian CY-37, and CY-55 simulations. The vectors near the left PVs, the right PVs, the LAA, and the mitral annulus are colored differently (cyan, dark blue, green, and red, respectively) to facilitate visualization. Also, magnified 3D vector maps inside the LAA, colored with the local value of blood velocity, are displayed. Snapshots corresponding to LA diastole, LV early filling, and LA systole are represented. The flow rate profiles in the pulmonary veins (PVs) and mitral annulus are also plotted together with the LA and LAA chamber volumes for reference.

In this healthy case, the atrial chamber expands significantly during atrial diastole (Figure 3A), driving a strong filling flow into the LA body and the LAA. During LV early filling (Figure 3B), the ventricular suction and elastic recoil of the atrium prompt the PVs and LAA to discharge blood into the LA body and, subsequently, into the LV. Atrial contraction (Figure 3C) keeps squeezing blood out of the LAA and the LA body and into the ventricle, but it also creates backflow from the LA into the PVs. Figure 4 shows flow snapshots for a patient with atrial fibrillation and an LAA thrombus, using the same format as Figure 3. In this patient, impaired atrial expansion leads to decreased filling flow during LA diastole, particularly in the LAA (Figure 4A). Ventricular suction creates strong fluid motion from the PVs into the ventricle during LV early filling; the LA mainly acts as a conduit during this phase (Figure 4B). Impaired LA contractility also reduces LAA and LA body draining into the LV during atrial systole (Figure 4C). In particular, the filling and drainage flows in the AF patient were weaker than in the healthy subject. Furthermore, the AF patient's LAA had a volume of 15.5 ml, which is much larger than the LAA of the healthy subject (4.85 ml, see Table 1), and its shape was less straight. Consequently, secondary swirling flows in the patient's LAA were more notable than in the healthy case.

For the most part, the overall flow patterns inside the LA body were not disturbed in the non-Newtonian CY-37 and CY-55 simulations. However, we found appreciable qualitative and quantitative differences inside the LAA, especially in the AF patient (Figures 3-4). First, the filling and drainage LAA jets were altered when non-Newtonian effects were considered. In the healthy subject (case 2), these differences were most noticeable during LV relaxation and atrial systole (Figure 3B-C). In the LAA-thrombus-positive AF patient (case 5), the differences were sustained throughout the cardiac cycle. Moreover, the secondary swirling motions in the AF patient's LAA showed significant alterations in the non-Newtonian simulations, including an important decrease of velocity magnitude (Figure 4).

3.2 Blood inside the left atrial appendage continuously experiences low shear rates consistent with non-Newtonian rheology

Reduced shear rates associated with slow blood flow inside the left atrial appendage (LAA) are thought to cause RBC aggregates, which manifest as spontaneous contrast in clinical echocardiographic acquisitions [39, 40]. Since low shear rates and RBC aggregates are hallmarks of non-Newtonian blood rheology, we analyzed the shear rate $S(\overrightarrow{x}, t)$ in in our simulations. Figure 5 shows instantaneous snapshots of $S(\overrightarrow{x}, t)$ from Newtonian and CY-37 simulations. The data come from a healthy subject (case 3), a patient with decreased LA reservoir function (case 4, history of TIAs), and a patient with decreased reservoir and booster functions (case 5, thrombus positive). The figure shows three representative phases of the cardiac cycle: left atrial (LA) diastole (left column), left ventricular (LV) early filling (center column) and LA systole (right column). To visualize LA vortices in the atrial body, we also represented iso-surfaces of the second invariant of the velocity gradient tensor $\left(Q = 1000\ \mathrm{s}^{-2}\right)$.

Given the relatively large Reynolds number and the unsteady nature of LA flow, the shear rate maps fluctuate in space and time. However, despite these fluctuations, $S(\overrightarrow{x}, t)$ remains low $\left(< 10\ \mathrm{s}^{-1}\right)$ in large portions of the LAA across the whole cardiac cycle. Since the CY-37 and CY-55 constitutive models yield $\nu/\nu_\infty = 1.3$ and 2 respectively at $S = 10\ \mathrm{s}^{-1}$ (see Figure 2A), the $S(\overrightarrow{x}, t)$ distributions from our simulations suggest that non-Newtonian effects could be considerable inside the LAA. The subjects with decreased atrial function had particularly low shear rates inside their LAA. These subjects also displayed low S regions inside the atrial body but these regions were not sustained over long times. The distributions of $S(\overrightarrow{x}, t)$ for Newtonian and CY-37 blood simulations were similar in that they produced low shear rates inside the LAA across the whole cardiac cycle. The LA vortex structures were qualitatively similar although there was a trend for non-Newtonian

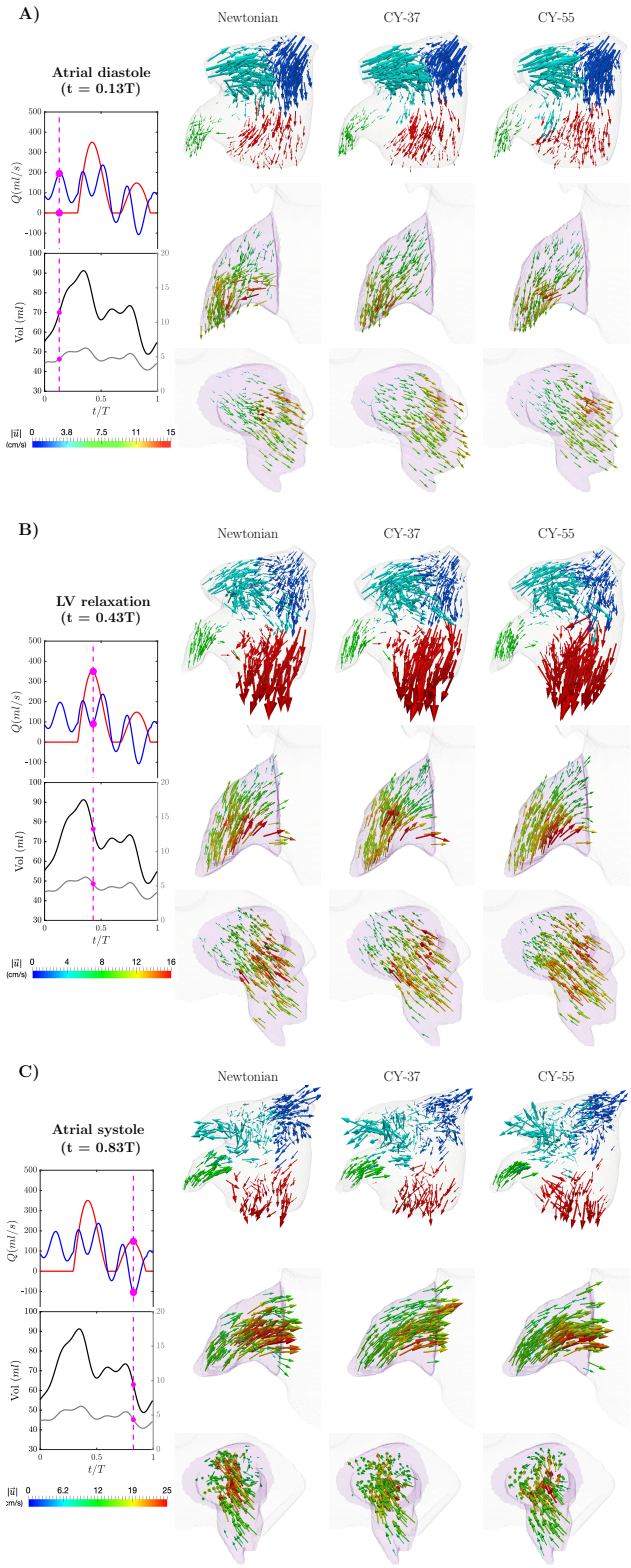

Figure 3: **Flow visualization of LA and LAA hemodynamics from Newtonian and non-Newtonian simulations. Subject with normal atrial function and no LAA thrombus.** Each panel displays a snapshot of the 3-D blood flow velocity in the whole LA (top) and two amplified views of the LAA in different orientations. In the top view, the vectors are colored according to their proximity to the right pulmonary veins (blue), left pulmonary veins (cyan), left atrial appendage (green) and mitral valve (red). In the bottom LAA views, the vectors are colored according to the velocity magnitude. The vectors in all views are scaled with the velocity magnitude. Each panel also includes time histories of the flow rate through the mitral valve (red) and the cumulative flow rate through the pulmonary veins (blue), and of the volumes of the left atrium (black) and the left atrial appendage (grey). The magenta bullets indicate the instant of time represented in the vector plots of each panel. The flow vectors inside the LA are represented at three instants of time. **A)** Atrial diastole and peak flow rate through the pulmonary veins (t = 0.13 s). **B)** Left ventricular diastole and peak flow rate through the mitral valve (E-wave, t = 0.43 s). **C)** Atrial systole and peak backflow rate through the pulmonary veins (t = 0.83 s).

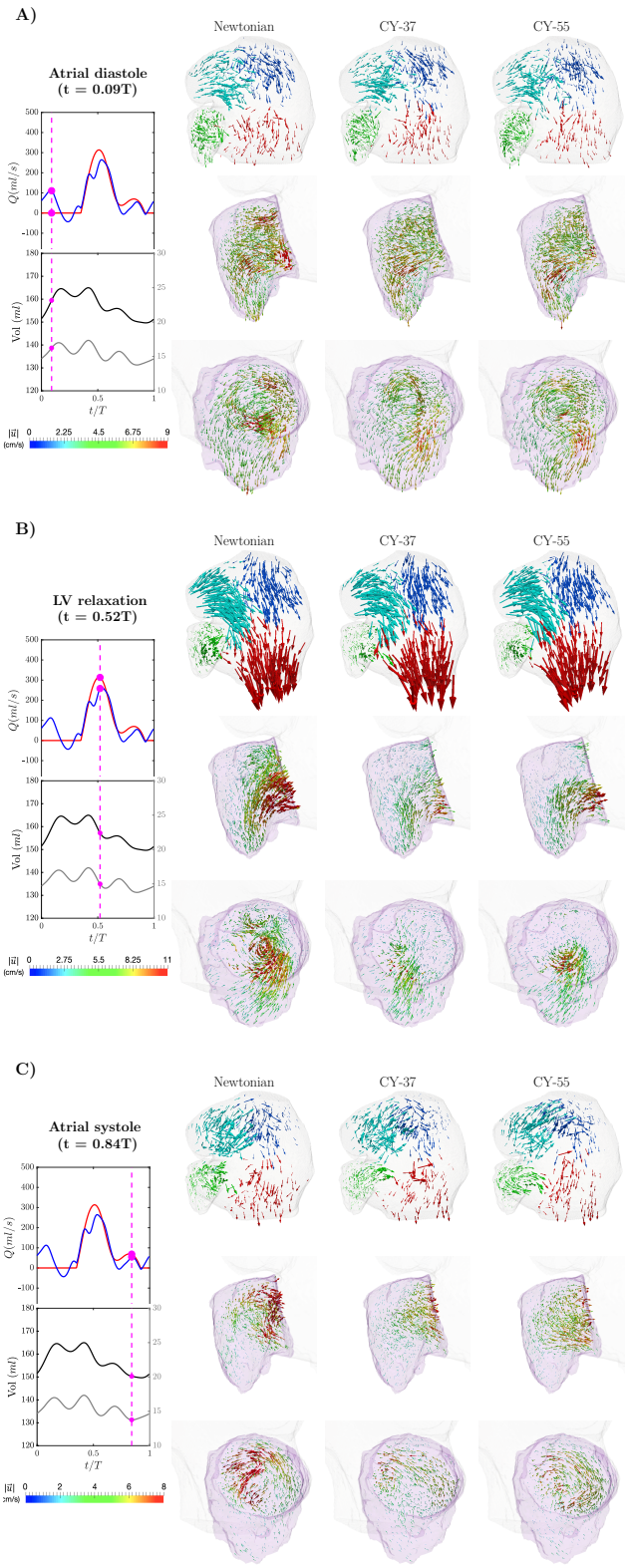

Figure 4: **Flow visualization of LA and LAA hemodynamics from Newtonian and non-Newtonian simulations. AF patient with LAA thrombus (digitally removed before running the simulations).** Vector maps of the 3-D blood flow velocity in the whole LA (top) and two amplified views of the LAA in different orientations, using the same format as Figure 3. **A)** Atrial diastole and peak flow rate through the pulmonary veins (t = 0.09 s). **B)** Left ventricular diastole and peak flow rate through the mitral valve (E-wave, t = 0.52 s). **C)** Atrial systole and peak backflow rate through the pulmonary veins (t = 0.84 s).

simulations to yield increased velocities along intense vortex cores.

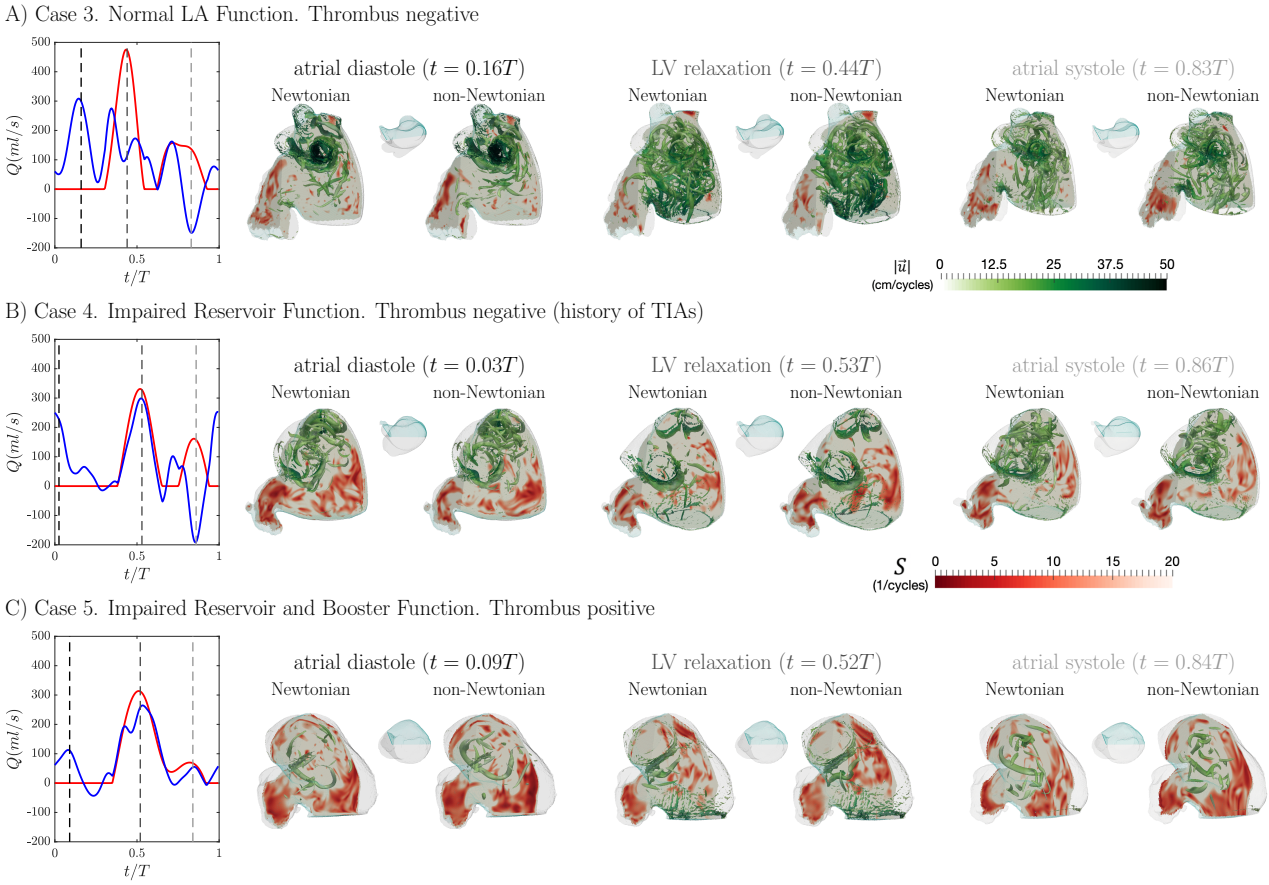

Figure 5: **Left atrial shear rate and vortex structures inside left atrium of subjects with or without LAA thrombus and with different atrial function.** Three subjects are shown, one without thrombus and normal atrial function (**panel A**), one with a history of TIAs and impaired reservoir function (**panel B**), and one with an LAA thrombus and both impaired reservoir and booster functions (**panel C**). Each panel includes plots of the time histories of flow rate through the mitral valve (red) and the cumulative flow rate through the PVs (blue). For each subject, instantaneous snapshots of the shear rate S are shown in two oblique plane sections of the LAA and the LA body, indicated the sagittal view insets. Additionally, the vortex patterns inside the LA are represented and colored according to the local velocity magnitude. Snapshots from both Newtonian and CY-37 simulations (Carreau-Yasuda model of eq. 3, $Hct = 37$) are included. These snapshots correspond to three instants of time: **1)** atrial diastole (*i.e.*, peak flow rate through the pulmonary veins), **2)** left ventricular rapid filling (*i.e.*, the E-wave, peak flow rate through the mitral valve), and **3)** atrial systole (*i.e.*, the A-wave of left ventricular filling and peak backflow rate through the pulmonary veins). These three instants of time are indicated with dashed vertical lines in the flow-rate plots at the left-hand-side of each panel.

3.3 Blood viscosity in Newtonian and non-Newtonian left atrial simulations

To evaluate the variations in atrial blood viscosity caused by the shear rate dependence and thixotropy of blood rheology, we determined the normalized time-averaged kinematic viscosity over the last three heartbeats of our simulations, $\langle \nu(\vec{x}) \rangle / \nu_\infty$, and mapped this quantity in two oblique intersecting plane sections of the LA body and the LAA (Figure 6A). In addition, we plotted time histories of the median and the 25th and 75th percentiles of ν/ν_∞ inside the LA body and LAA $\left[\overline{\nu(t)}/\nu_\infty, \text{Figure 6B}\right]$, and the probability density function of ν/ν_∞ inside the LAA averaged in the last simulated cycle (Figure 6C). Consistent with the sustained presence of low-shear regions inside the left atrium, the CY-37 and CY-55 simulations had higher kinematic viscosity than the Newtonian simulation. The low-hematocrit CY-37 simulations (Figure 6, 1st column) produced moderate increases in viscosity for healthy subjects (range 1.18-1.25, Table 2), which were mostly confined inside the LAA. There was a trend for the CY-37 simulations to produce higher increases in viscosity in AF patients (range 1.31-1.38, Table 2) than in healthy ones, with more extensive zones of elevated $\langle \nu(\vec{x}) \rangle / \nu_\infty$ inside the LAA and

and the LA body. The high-hematocrit CY-55 simulations (Figure 6, 3rd column) produced significantly larger viscosity values all over the LA body and LAA $\langle \nu(\vec{x}) \rangle / \nu_\infty = 1.99$ and 2.56 for the healthy and AF patients simulated, Table 2).

Viscosity model	ν_0	ν_∞	Hct	λ	a	n	T_μ (s)	σ (s)	Cases	$\langle S(\vec{x}) \rangle$ (s^{-1})	$\langle \nu(\vec{x}) \rangle / \nu_\infty$	$\langle T_R(\vec{x}) \rangle$(s)	$\frac{\langle T_R^{NN}(\vec{x}) \rangle - \langle T_R^{N}(\vec{x}) \rangle}{\langle T_R^{N}(\vec{x}) \rangle}$ (%)	$\langle T_{R,max}(\vec{x}) \rangle$ (s)	$\%Vol\ T_R > 6s$	$\%Vol\ T_R > 8s$	$\%Vol\ T_R > 10s$
Newtonian	0.64	0.04	-	-	-	-	-	-	1	23.85	1.00	2.27	-	8.83	8.29	0.54	0.00
CY			37	8.2	0.64	0.2128	-	-	1	22.93	1.18	2.87	26.91	13.63	28.61	12.46	3.53
Newtonian			-	-	-	-	-	-	2	21.04	1.00	1.63	-	7.04	1.39	0.00	0.00
CY			37	8.2	0.64	0.2128	-	-	2	17.87	1.24	1.99	22.63	9.71	9.83	2.27	0.24
CY			55	3.313	2	0.3568	-	-	2	16.97	1.99	2.12	30.54	11.37	19.49	8.81	1.97
CY$-T_R$			37	8.2	0.64	0.2128	3	0.6	2	18.98	1.04	1.83	12.29	8.94	3.22	0.41	0.00
CY$-T_R$			55	3.313	2	0.3568	3	0.6	2	18.89	1.15	2.12	30.54	8.98	5.41	0.63	0.00
Newtonian			-	-	-	-	-	-	3	17.42	1.00	2.30	-	9.59	13.95	4.48	0.00
CY			37	8.2	0.64	0.2128	-	-	3	17.87	1.25	3.06	33.07	12.93	33.39	22.84	12.06
Newtonian	0.64	0.04	-	-	-	-	-	-	4	11.03	1.00	3.25	-	11.53	34.35	16.45	5.45
CY			37	8.2	0.64	0.2128	-	-	4	11.66	1.31	4.30	32.59	17.83	40.58	32.42	24.26
Newtonian			-	-	-	-	-	-	5	9.73	1.00	3.88	-	10.88	25.58	12.50	2.37
CY			37	8.2	0.64	0.2128	-	-	5	8.29	1.38	4.01	3.23	16.06	26.40	13.62	7.25
CY			55		2	0.3568	-	-	5	7.33	2.56	4.65	19.72	17.44	34.58	23.43	17.44
CY$-T_R$			37	8.2	0.64	0.2128	3	0.6	5	7.52	1.27	4.00	3.06	18.03	21.06	12.47	7.01
CY$-T_R$			55	3.313	2	0.3568	3	0.6	5	7.87	1.92	4.45	14.79	16.48	38.49	25.59	14.19
Newtonian			-	-	-	-	-	-	6	12.16	1.00	2.53	-	7.76	4.84	0.00	0.00
CY			37	8.2	0.64	0.2128	-	-	6	12.09	1.34	2.55	0.71	8.94	8.85	0.57	0.00
										LAA				distal LAA			

Table 2: **Summary of blood rheology models and cases studied, including time-averaged hemodynamical statistics evaluated in the left atrial appendage (LAA) and the distal LAA.** *hct*, hematocrit level; Carreau-Yasuda model parameters (ν_0, ν_∞, λ, a and n), and modified Carreau-Yasuda model additional parameters (T_μ and σ), see section 2.3 for description; $\%Vol\ T_R > \tau$, percentage of volume with residence time larger than the time threshold τ. Metrics between $\langle\ \rangle$ are time averages over the phase-averaged cardiac cycle obtained in the three cycles highlighted with a grey shaded region in Figures 6 and 7.

Previous Newtonian CFD analyses including our own [35] suggest that LA blood residence time can be comparable to the timescale associated to blood's thixotropic behavior [58, 57]. Thus, the CY-55 and CY-37 models, which assume steady state blood rheology, could overestimate blood viscosity in regions of low blood residence time. To investigate how the competition between RBC aggregation kinetics and flow unsteadiness influences the results of the CFD analysis, we ran the two patient-specific cases of Figure 1 using the low CY-T_R-37 and high-hematocrit CY-T_R-55 constitutive laws (eqs. 4- 5). In these thixotropic constitutive relations, non-Newtonian effects only kick in if the local residence time is longer than the activation time $T_\mu = 3$ s. Consistent with this T_R-dependent activation, the CY-T_R-55 model yielded viscosities that were very close to the constant Newtonian reference value inside the whole LA body and in the proximal part of the LAA (4th column of Figure 6). In contrast, the CY-55 model yielded significantly higher viscosity values with $\langle \nu(\vec{x}) \rangle / \nu_\infty = 1.68$-2.42 in the LA body. The same trend was observed when comparing the CY-T_R-37 and CY-37 simulations, although the effect of considering T_R-dependent activation was attenuated due to the smaller viscosities present prescribed by the constitutive law at low-hematocrit. The next section characterizes how the viscosity variations caused by the constitutive laws we investigated (*i.e.* CY-37, CY-55, CY-T_R-37, and CY-T_R-55) affect the predictions of blood stasis from the CFD analysis.

3.4 Blood stasis in Newtonian and non-Newtonian left atrial simulations

We examined how non-Newtonian blood rheology affects LAA blood stasis by mapping the blood residence time obtained with the CY-37, CY-55 constitutive laws, and comparing it to the constant viscosity results of Garcia-Villalba et al. [35]. The T_R maps indicate that most of the LA body's blood pool is cleared and replenished every 1-2 cardiac cycles ($T_R \leq 2$ s, grey shades in Figure 7A). On the other hand, the LAA residence time can reach large values, particularly in the LAA regions most distal from the ostium (Figure 7A). The increase in residence time between the LA body and the appendage was larger in patients with impaired atrial function (Figure 7B), whose LAA contracted and expanded weaklier than those of healthy subjects (see LA functional parameters in Table 1). The LAA was also the site where the residence time maps produced by non-Newtonian simulations differed most from the Newtonian ones. These results are consistent with our findings that non-Newtonian effects are most significant inside the LAA (Figure 6), and that these effects weaken the filling, drainage, and stirring of blood inside this chamber (Figures 3 and 4). The CY-37 and CY-55 simulations exacerbated high-T_R stagnant regions by augmenting their size and maximum residence time. Conversely, regions of moderate or low-T_R were not affected as much. These differences were significant even in the low hematocrit simulation, CY-

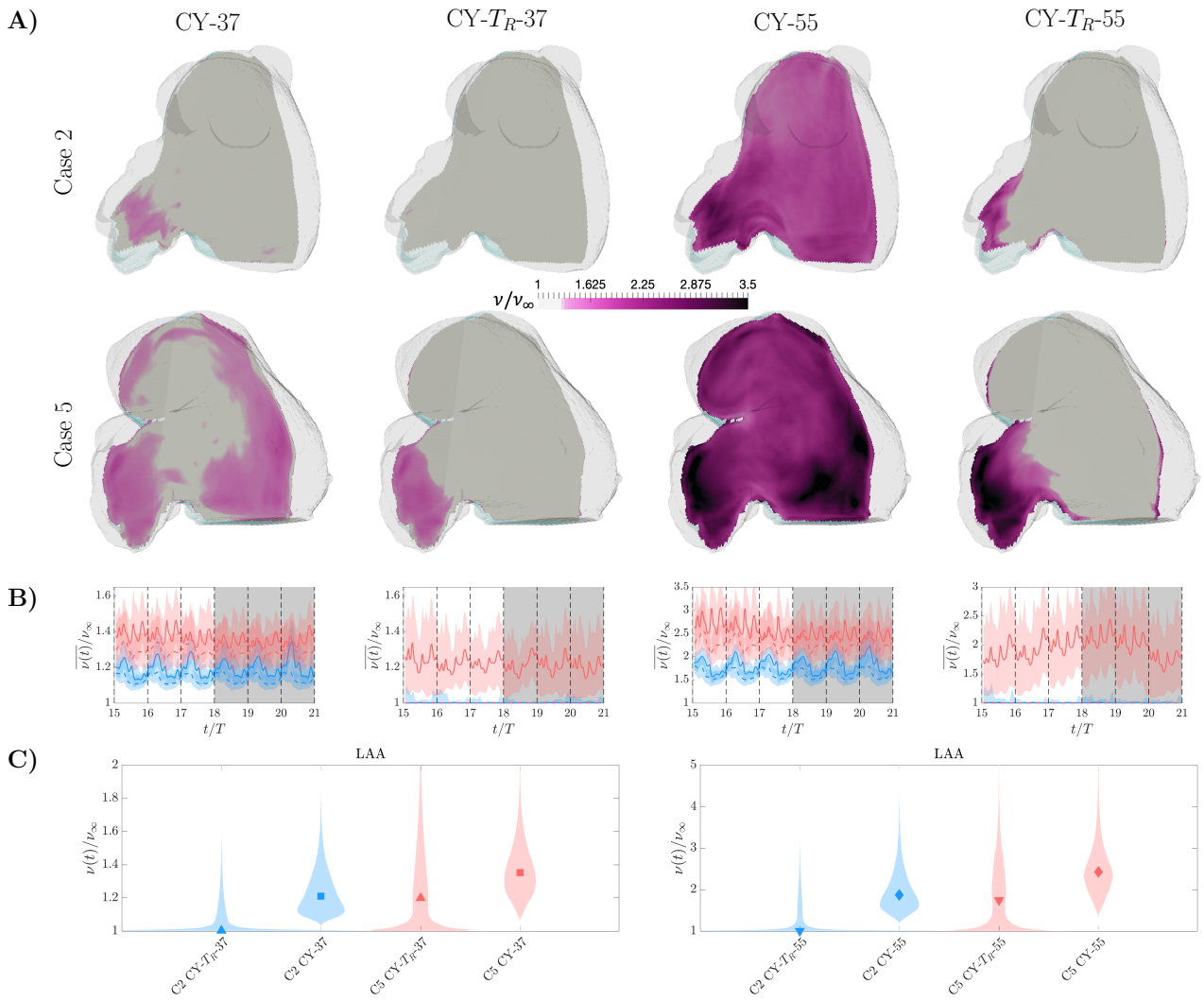

Figure 6: **Left atrial viscosity for non-Newtonian different constitutive laws.** **A)** Spatial distribution of kinematic viscosity. Two subjects are shown, one without thrombus and normal atrial function (**top**), and one with an LAA thrombus (digitally removed before running the simulations) and both impaired reservoir and booster functions (**bottom**). For each subject, the time-averaged, normalized viscosity $\langle \nu(\vec{x}) \rangle / \nu_\infty$ is shown in two oblique plane sections of the LAA and the LA body, similar to Figure 5. Data from simulations with low-hematocrit CY-37 (1st column), low-hematocrit, residence-time-activated CY-T_R-37 (2nd column), high-hematocrit CY-55 (3rd column), and high-hematocrit, residence-time-activated CY-T_R-55 (4th column) constitutive laws are included. **B)** Time histories of kinematic viscosity from the healthy, thrombus-negative subject (blue) and the thrombus-positive patient with AF shown in **panel A**. Data from the last 6 cycles of the simulations are plotted, with the grey shaded region indicating the three cycles used to calculate time averages (*i.e.*, $\langle \nu(\vec{x}) \rangle / \nu_\infty$ in **panel A** and **panel C**). Lines represent the median and colored shaded regions are plotted between the 25th and 75th percentiles. Solid lines indicate the LAA while dashed lines indicate the LA body. **C)** Violin plots of the probability density function (shaded patches) inside the LAA, together with the median (symbol).

37, and became more pronounced in the high hematocrit case, CY-55. For instance, the apical LAA residence times predicted by the CY-37 simulation for the healthy and AF cases of Figure 7 were 38% and 48% higher than their Newtonian values, respectively, whereas these differences were 62% and 60% when considering the CY-55 constitutive law.

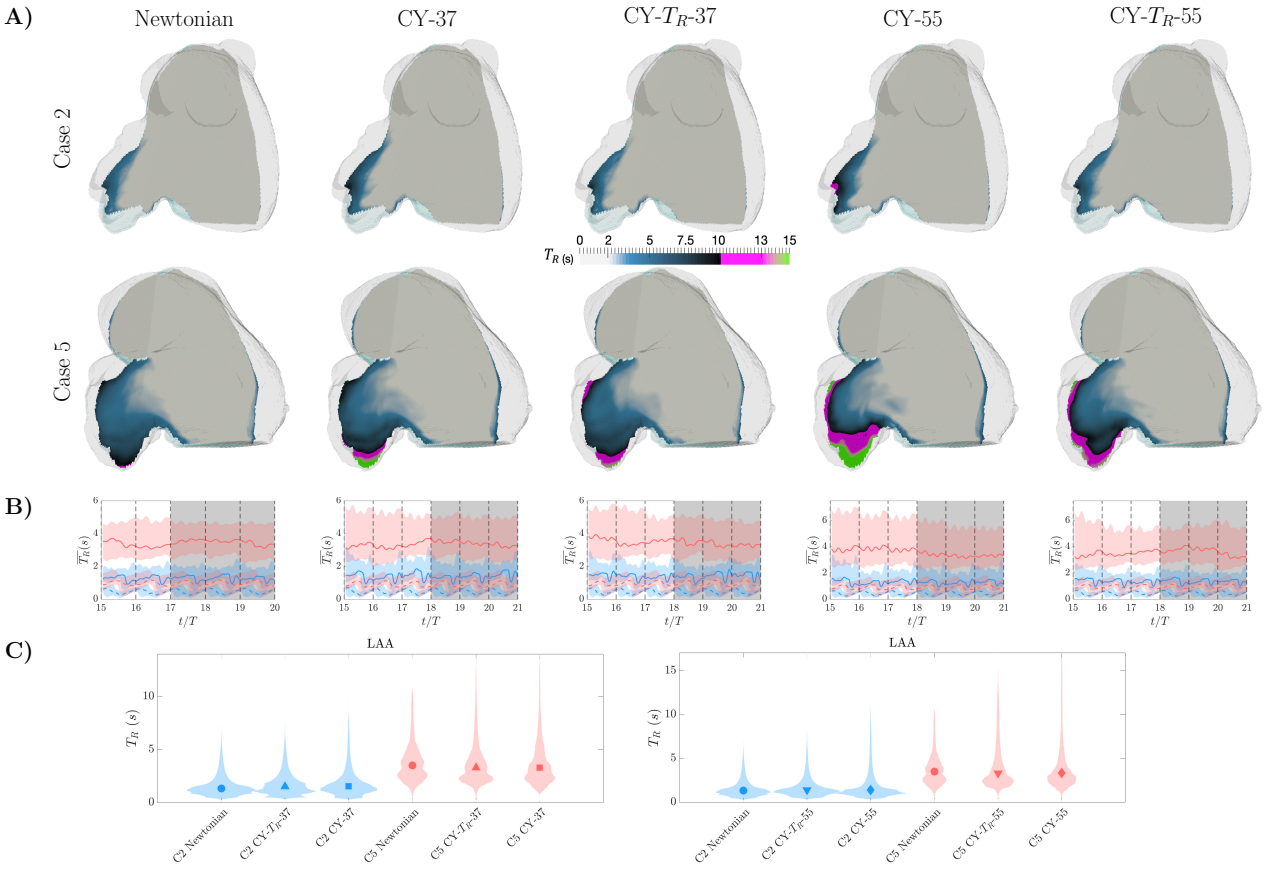

Figure 7: **Left atrial blood residence time for non-Newtonian different constitutive laws.** Panels of this Figure are presented in the same format as Figure 6, but including Newtonian results in the left column. **A)** Spatial distribution of residence time. **B)** Time histories of residence time inside the LA body and the LAA. **C)** Violin plots of the probability density function inside the LAA.

As expected, the thixotropic non-Newtonian simulations (CY-T_R-37, CY-T_R-55) predicted lower LAA residence time values than their equilibrium counterparts (CY-37, CY-55). However, the situation was different in the LA body, where all non-Newtonian simulations yielded similar results for T_R. This result is not intuitive, given that residence remained below the non-Newtonian activation timescale (*i.e.*, $T_R < T_\mu$) inside the LA body, so that non-Newtonian effects were not triggered. Furthermore, the residence time in the Newtonian simulations was also similar to that of the thixotropic and equilibrium non-Newtonian ones. In the discussion section, we argue that these results imply that the LA body's clearing and replenishing are mainly dictated by mass conservation, independent of blood viscosity.

To quantify how non-Newtonian rheology influenced blood stasis estimations from our patient-specific simulations, we focused on the distal LAA, the region with maximum residence time where where thrombi are most likely to form. Specifically, we considered the 50% voxels inside the LAA that were most distant from the ostium and computed the percentage of those voxels occupied by stagnant blood, defined as T_R larger than several cutoff values (6, 8, 10 s). Consistent with Figure 7A, the fraction of the distal LAA that was predicted to be stagnant increased notably when non-Newtonian effects were considered. Table 2 shows that, when comparing the low-*Hct* model CY-37 with the reference Newtonian simulations, the blood stagnant volume in the distal LAA increased from 8% to 24% on average for healthy subjects and from 22% to 25% for AF patients for moderate cutoff values (6 s), whereas it increased from 0% to 5% in healthy subjects and from 2.6% to 11% in AF patients for high cutoff values (10 s). Likewise, the maximum residence increased from 8.1 to 12 on average

for healthy subjects and from 10 to 14 for AF patients. In addition, both the stagnant distal LAA volume and the maximum residence time increased with *Hct* for a given given constitutive law (*i.e.*, CY-37 with CY-55 and CY-T_R-37 with CY-T_R-55). Overall, these results suggest that neglecting non-Newtonian rheology can lead to underestimating the size of stagnant regions inside the LAA as well as their level of stasis.

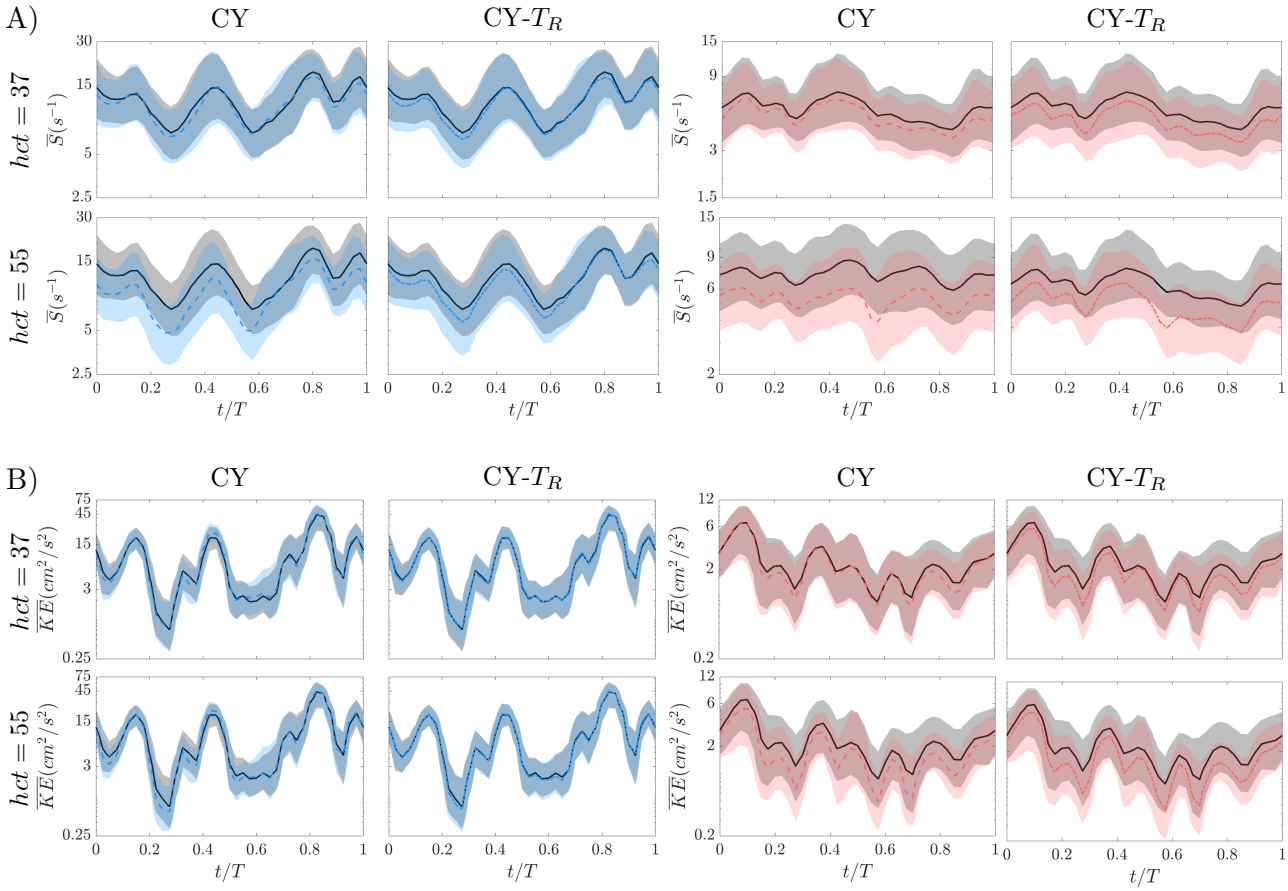

Figure 8: **Shear rate and Kinetic energy in the distal LAA for Newtonian and non-Newtonian different constitutive laws. A)** Time histories during one cardiac cycle of shear rate median and 25th-75th percentiles (denoted by colored shaded regions). The subject with normal atrial function (case 2) is represented with blue lines and patches, and the subject with an LAA thrombus and abnormal atrial function (case 5) is depicted in red. The four non-Newtonian constitutive laws are included for each case: *Hct* changes between rows and the constitutive models between columns. Median and 25th-75th percentiles of Newtonian case for the same patient are also included in black for comparison. **B)** Time histories during one cardiac cycle of kinetic energy median and 25th-75th percentiles. Panels are presented in the same format than in **A)**.

Two other metrics commonly used in CFD analyses to summarize cardiac hemodynamics and, in particular, stasis are the flow mean shear rate S and the kinetic energy, $\mathrm{KE} = (\vec{u} \cdot \vec{u})/2$, respectively. Figure 8 displays the median together with the 25th and 75th percentiles of these two variables inside the LAA along one cycle (phase-averaged for the three last cycles of the simulations, *i.e.*, the shaded in grey in Figure 6B and Figure 7B). Data are shown for a subject with normal atrial function (blue, left panels) and an AF patient with an LAA thrombus (red, right panels). Simulations results from the constitutive relations CY-37, CY-55, CY-T_R-37, and CY-T_R-55 are plotted together with those from the reference Newtonian simulations (grey). In both subjects, non-Newtonian effects moderately shifted the distributions of S and KE towards lower values of these variables. In the healthy subject, the shift was most pronounced during the atrial diastole and systole, while it was barely detectable during LV relaxation. In the AF patient, the shift towards lower S and KE was sustained throughout the whole cardiac cycle. The contrast between the large increase of T_R and the moderate differences in S or KE supports the idea that velocity changes accumulating over multiple heartbeats can significantly impact residence time and blood stasis.

4 Discussion

The left atrial appendage (LAA) is regarded as the most likely thrombosis site in patients with AF who suffer embolic strokes [59, 60]. Sustained low shear leading to increased blood viscosity could cause hemodynamics alterations and magnify LAA blood stasis [33, 35], a critical factor in thrombogenesis [61]. This study aimed to evaluate how non-Newtonian rheology could affect left atrial (LA) hemodynamics and CFD-derived metrics of LAA blood stasis, particularly residence time. Since Shettigar *et al.* [62] reported blood residence time to examine the washout of artificial ventricles, this quantity has been used to study the efficiency of blood transport in the cardiac chambers [63, 48, 64] and, more specifically, the risk of intracardiac thrombosis [13, 65, 35, 66, 28]. Patient-specific computational fluid dynamics (CFD) analyses are emerging as a tool to help assess LAA thrombosis risk [6, 35, 67]. However, previous investigations have considered constant fluid viscosity, neglecting the non-Newtonian rheology of blood at low shear rates [68].

4.1 Red blood cell aggregation in the LAA

Red blood cell (RBC) aggregation into rouleaux is a significant cause of non-Newtonian blood rheology at low shear rates and long residence times. There is ample clinical evidence of RBC aggregation in the left atrium because RBC rouleaux increase blood's echogenicity creating spontaneous contrast (a.k.a. "smoke") [39]. Multiple studies have established a relationship between LAA blood stasis, echocardiographic "smoke", and the risk of LAA thrombosis, especially in patients with AF [69, 70, 71, 72, 61, 73, 74]. Moreover, previous CFD analyses of LA hemodynamics consistently report shear rates below 70 s^{-1} and residence times above 5 s inside the LAA, which, according to data from in vitro experiments, should cause RBC aggregation [33, 35, 67, 68]. However, there is a lack of studies evaluating the importance of non-Newtonian blood rheology in the LA and LAA hemodynamics. Recently, Wang *et al.* [75] incorporated non-Newtonian effects in their CFD simulations of blood flow of a patient-specific LA model. Yet, these authors did not specifically focus on non-Newtonian effects; instead, they investigated how beating rhythm can affect the risk of thrombosis.

4.2 The range of Non-Newtonian effects: effects of hematocrit and rouleaux formation kinetics

We considered constitutive relations based on the Carreau-Yasuda model (eq. 3), which has been extensively used in previous CFD analyses of cardiovascular flows outside of the LA [76, 77, 27]. The Carreau Yasuda model depends on several parameters that are sensitive to the hematocrit level (Hct). Hematocrit, the blood's volume fraction occupied by RBCs, is a major determinant of blood viscosity together with flow shear rate [36]. Normal hematocrit levels can vary among individuals within the range $Hct = [34, 54]$ depending on factors like age and sex [55, 56]. Thus, to evaluate the extent of potential non-Newtonian effects, we parameterized the Carreau-Yasuda model using values from the literature corresponding to $Hct = 37$ and $Hct = 55$ [52, 53]. These simulations, which we denoted CY-37 and CY-55, allowed us to probe non-Newtonian effects for the lower and upper limits of the normal Hct range. They yielded increased blood viscosity inside the LA chamber as compared to the Newtonian simulations. The differences were especially significant inside the LAA, where the normalized average viscosity (*i.e.*, $\overline{\nu(\overrightarrow{x}, t)}/\nu_\infty$) ranged between [1.14–1.58] for $Hct = 37$ and [1.64–3.47] for $Hct = 55$. These viscosity amplifications are consistent with those reported in CFD analyses of other vessels and cardiac chambers [27, 77].

The Carreau-Yasuda model presumes that rouleaux formation exclusively depends on shear rate, which is a reasonable assumption for quasi-steady flows in small vessels with simple tubular geometries (*e.g.*, the microcirculation). In these geometries, the flow timescales are longer than those of RBC aggregation kinetics, and low shear rate implies flow separation and high residence time. However, these assumptions break down for the complex, unsteady flows observed in the cardiac chambers [63]. In vitro investigations of rouleaux formation kinetics have reported RBC aggregation times between 3 and 15 s for normal blood and between 0.5 and 1.5 s for pathologically hypercoagulable blood [57, 58, 78, 79]. To consider the interplay between these timescales and the flow timescales induced by cardac pulsatility, we ran simulations with a thixotropic constitutive relation. Specifically, we implemented a modified constitutive relation that progressively activates the Carreau-Yasuda model as residence time increases beyond $T_\mu = 3$ s (eqs. 4-5) [37]. We considered hematocrit levels $Hct = 37$ and $Hct = 55$ and denoted the corresponding simulations CY-T_R-37 and CY-T_R-55. These simulations produced viscosities close to the Newtonian reference value inside the LA body, which is replenished every 1-2 heartbeats. However, the LAA remained a site of significant non-Newtonian rheology, showing normalized average viscosi-

ties of up to $\left[\nu(\vec{x},t)\right]_{max}/\nu_\infty = 1.4$ and 2.8 in the CY-T_R-37 and CY-T_R-55 cases considered, respectively. Our observations in the LAA contrast with the finding that considering the kinetics of rouleaux formation notably decreased shear-thinning effects in abdominal aortic and intracranial aneurysms [37]. We attribute this difference to the fact that blood residence time inside the LAA seems to be considerably longer than in aneurysms [37, 80].

4.3 Effects of non-Newtonian rheology on LA and LAA hemodynamics and blood residence time

There is little information about the influence of blood's shear-thinning rheology on intracardiac hemodynamics. In the LV, clinical observation of echocardiographic "smoke" suggest RBC aggregates can form in this chamber [81, 82], and two modeling studies have evaluated non-Newtonian effects. Doost *et al.* used CFD analysis to evaluate various constitutive relations on a patient-specific LV anatomical model, finding that blood viscosity increased strongly in the apical region [77]. More recently, Riva *et al.* analyzed patient-specific 4-D flow MRI and *Hct* measurements, reporting significant deviations from Newtonian behavior in areas of recirculating or low velocity [83]. It should be noted that Doost *et al.*'s constitutive models correspond to high hematocrit (*e.g.*, their Carreau model is equivalent to the present CY-55 model). Moreover, both Doost *et al.* and Riva *et al.* neglected the kinetics of rouleaux formation. Yet, blood flow tends to be slowest and residence time tends to be highest near the LV apex [84], and these features are exacerbated after acute myocardial infarction [13]. Overall, the existing data suggest that non-Newtonian effects in the LV might be appreciable in some pathological conditions.

The influence of blood's shear-thinning on atrial hemodynamics is even more understudied than in the LV; we are unaware of previous flow imaging studies, and we are only aware of the beforementioned CFD study of Wang *et al.* [75]. Inside the atrial body, our Newtonian and non-Newtonian simulations produced similar flow patterns for all the constitutive models considered, even if viscosity significantly increased throughout the whole chamber for the CY-55 model. Likewise, T_R inside the LA body was not appreciably affected by blood's shear thinning. One can explain this behavior by considering that the main flow pattern in the LA body consists of approximately straight motion from the PVs to the mitral annulus. This flow pattern is mainly dictated by global mass conservation in our simulations, whose boundary conditions drive a fluid volume equal to the LV stroke volume (LVSV) through the LA body every heartbeat. Consequently, the mean T_R inside the LA body could be roughly approximated as $T_{R,LA-body} \approx LAV/\left(\alpha LVSV\right)$ cycles, where LAV is the mean LA volume and the factor $\alpha > 1$ in the denominator accounts for most of the transport occurring during the E wave, which only spans a fraction of the cycle. While this estimation neglects relevant details such as the E/A ratio or the LA's reservoir and booster functions, Figure SI 1 indicates that it is a good approximation for $\alpha \approx 2$, supporting that T_R in the LA body is indeed dictated by global chamber mass conservation, at least in our simulations. Thus, since the LA volume, LVSV, and E/A ratio were the same in our Newtonian and non-Newtonian simulations, the overall distribution of T_R in the atrial body was not significantly altered by implementing different constitutive laws (Figure 2).

In contrast to the LA body, the LAA is a closed chamber excluded from the atrium's blood transit conduit that needs multiple heartbeats to be cleared and replenished. The filling and drainage jets driven by the expansion and contraction of the LAA walls play an important role in recycling the LAA's blood pool. The net flow rate these jets create through the LAA's orifice is dictated by the time rate of change of LAA volume and should be relatively insensitive to variations in blood viscosity. However, we and other have demonstrated the existence of significant secondary swirling flows inside the LAA [35], which can also transport blood into and out of the LAA even if their associated net flux is zero. In fact, we previously showed that fixed-wall simulations and moving-wall simulations produce comparable values of blood residence time inside LAAs of the same geometry [35]. Furthermore, while previous CFD analyses indicate that LAA residence time correlates inversely with the LAA ejection fraction [35], this correlation is imperfect and additional factors such as LA volume, LAA morphology, PV flow profiles, and MV have been shown to vortical patterns and residence time inside the LAA [32, 51]. Of note, LAA morphology is a well-known stroke risk factor in patients with AF [12]. Our non-Newtonian simulations suggest that the blood shear thinning not only can affect the shape of the filling and draining jets but also dampen the secondary swirling motions inside the whole appendage. These differences translate into larger values of LAA residence time when non-Newtonian blood rheology is considered, especially in the distal region near the LAA apex.

Considering different constitutive laws and hematocrit values proved helpful to evaluate the influence of non-Newtonian effects in LAA residence time. In the cases studied, the time-averaged LAA T_R increased by up to

33%, and and the maximum value of T_R increased by up to 66%. Furthermore, significantly larger volumes within the LAA presented high values of T_R when non-Newtonian effects were considered (*e.g.*, the volume with $T_R > 6$ s increased by up to 14 fold). Overall, our CFD analyses suggest that non-Newtonian blood rheology significantly impact the predicted values of LAA residence time, even for values within the normal range. Moreover, our data suggest that LAA blood stasis is exacerbated by high hematocrit, consistent with clinically observed associations between hematocrit and the incidence of ischemic stroke, especially in males and the aged [85, 86], who have higher hematocrit than other demographic groups. We did not observe a trend for non-Newtonian effects on T_R to be stronger in normal or AF subjects. This result is consistent with the notion that secondary flows not driven by atrial wall motion are most affected by blood shear thinning. However, given the small size of our cohort, further studies would be required to tackle this question more definitely. Large studies could also address whether non-Newtonian effects could be more prominent depending on LAA morphology.

4.4 Study Limitations

As mentioned above, the size of our subject cohort was too small ($N = 6$) to statistically infer or discard potential correlations between non-Newtonian effects and LA/LAA function or geometry. Nevertheless, the cohort included subjects with normal LA function and a variety of LA dysfunctions (*e.g.*, reservoir and/or booster pump) as well as subjects in sinus rhythm and with AF. Thus, our analyses demonstrate the potential impact of non-Newtonian blood rheology in LA hemodynamics and LAA residence time for a wide range of patient-specific settings.

We did not input patient-specific values of heart rate in our simulations. Instead, we ran all our cases at 60 beats per minute, similar to Garcia-Villalba *et al.*'s [35] constant viscosity simulations, which we used as the Newtonian baseline in the present study. Heart rate is known to influence both the shear rates and residence time in the left ventricle [87, 88], and similar dependencies are anticipated in the LA. Future studies shall address whether these phenomena cause non-Newtonian effects in the LAA to be heart-rate dependent. We did not consider patient-specific hematocrit values. Instead, we ran simulations for two hematocrit values near the lower and upper limits of this parameter's normal range with the goal of assessing the potential extent of non-Newtonian effects. Likewise, the characteristic time (T_μ) in our thixotropic constitutive laws was selected to be 3 seconds for all subjects based on human RBC aggregation times measured in vitro by different techniques [58, 78, 57, 79]. We implemented patient-specific inflow/outflow boundary conditions, with the caveat that the PV flow rates were evenly distributed to match the boundary conditions used in Garcia-Villalba et al.'s [35] Newtonian baseline simulations. A 40%-60% split between the left and right pulmonary veins seems more physiological, although it does not produce significantly different LA hemodynamics than the 50%-50% split [29, 51]. We did not model the mitral valve as is customary in CFD analyses of LA hemodynamics [30, 89, 31, 32, 33]. The rationale for this simplification is that whole left heart simulations including the mitral valve do not suggest that this valve does not significantly affect LA flow [17, 16].

It should be noted that our simulations are driven by mass flux boundary conditions so that a fluid volume equal to the patient specific LVSV transits the atrium every heartbeat. This choice implies that the external work performed by the LA varies when the blood's constitutive relation is varied for each subject. However, the pressure drop between the PVs and the MV changes less than 0.3 mmHg between our Newtonian and non-Newtonian simulations, which is negligible compared to the total pressure in the LA (10 mmHg, see [90, 91, 92].

5 Conclusions

Patient-specific CFD analyses of left atrial hemodynamics suggest that the thixotropic, shear-thinning rheology of blood can significantly affect flow patterns inside the atrial appendage in a hematocrit-dependent manner. These non-Newtonian effects, which were largely neglected in previous CFD studies, aggravate blood stasis and could increase the likelihood of left atrial appendage thrombosis, a recognized risk factor in ischemic stroke.

Acknowledgements. This work was supported by American Heart Association Grant 20POST35200401 (Alejandro Gonzalo Grande).

Supplementary information (SI)

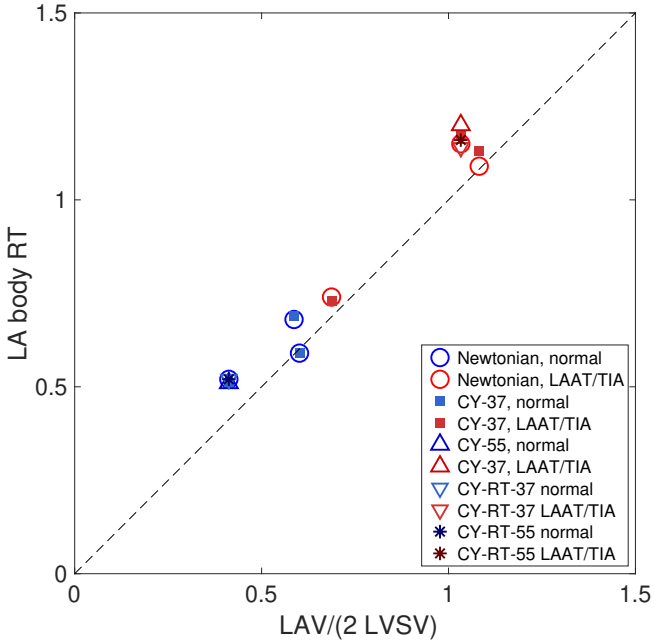

Figure SI 1: **Model to predict T_R inside of the LA body.** Residence time (T_R) approximation based on the mean LA volume (LAV), the LV stroke volume (LVSV), and a factor α that accounts for the fraction of the cycle the E wave spans. Symbols identify the average value obtained for subjects with normal LA function (normal) cases and subjects with LAA thrombus or a history of TIAs (LAAT/TIA) with each viscosity model used (see Table 2).

References

[1] Salim S Virani, Alvaro Alonso, Emelia J Benjamin, Marcio S Bittencourt, Clifton W Callaway, April P Carson, Alanna M Chamberlain, Alexander R Chang, Susan Cheng, Francesca N Delling, et al. Heart disease and stroke statistics—2020 update: a report from the american heart association. *Circulation*, 141(9):e139–e596, 2020.

[2] Emelia J Benjamin, Paul Muntner, Alvaro Alonso, Marcio S Bittencourt, Clifton W Callaway, April P Carson, Alanna M Chamberlain, Alexander R Chang, Susan Cheng, Sandeep R Das, et al. Heart disease and stroke statistics—2019 update: a report from the american heart association. *Circulation*, 139(10):e56–e528, 2019.

[3] Lung-Chun Lin, Yi-Lwun Ho, Shian-Li Kao, Chau-Chung Wu, Chiau-Song Liau, and Yuan-Teh Lee. Power doppler-derived speckle tracking image of intraventricular flow in patients with anterior myocardial infarction: correlation with left ventricular thrombosis. *Ultrasound Med Biol*, 26(2):341–346, 2000.

[4] Robert G Hart, Hans-Christoph Diener, and Stuart J Connolly. Embolic strokes of undetermined source: support for a new clinical construct–authors' reply. *Lancet Neurol*, 13(10):967, 2014.

[5] Hooman Kamel, Peter M Okin, Mitchell SV Elkind, and Costantino Iadecola. Atrial fibrillation and mechanisms of stroke: time for a new model. *Stroke*, 47(3):895–900, 2016.

[6] Patrick M Boyle, Juan Carlos Del Álamo, and Nazem Akoum. Fibrosis, atrial fibrillation and stroke: clinical updates and emerging mechanistic models. *Heart*, 107(2):99–105, 2021.

[7] Christopher A Aakre, Christopher J McLeod, Stephen S Cha, Teresa SM Tsang, Gregory YH Lip, and Bernard J Gersh. Comparison of clinical risk stratification for predicting stroke and thromboembolism in atrial fibrillation. *Stroke*, 45(2):426–431, 2014.

[8] Robert G Hart, Mukul Sharma, Hardi Mundl, Scott E Kasner, Shrikant I Bangdiwala, Scott D Berkowitz, Balakumar Swaminathan, Pablo Lavados, Yongjun Wang, Yilong Wang, et al. Rivaroxaban for stroke prevention after embolic stroke of undetermined source. *N Engl J Med*, 378(23):2191–2201, 2018.

[9] Wern Yew Ding, Dhiraj Gupta, and Gregory YH Lip. Atrial fibrillation and the prothrombotic state: revisiting virchow's triad in 2020. *Heart*, 106(19):1463–1468, 2020.

[10] Günther Ernst, Claudia Stöllberger, Friedrich Abzieher, Walter Veit-Dirscherl, Elisabeth Bonner, Brigitte Bibus, Barbara Schneider, and Jörg Slany. Morphology of the left atrial appendage. *Anat Rec*, 242(4):553–561, 1995.

[11] NM Al-Saady, OA Obel, and AJ Camm. Left atrial appendage: structure, function, and role in thromboembolism. *Heart*, 82(5):547–554, 1999.

[12] Luigi Di Biase, Pasquale Santangeli, Matteo Anselmino, Prasant Mohanty, Ilaria Salvetti, Sebastiano Gili, Rodney Horton, Javier E Sanchez, Rong Bai, Sanghamitra Mohanty, et al. Does the left atrial appendage morphology correlate with the risk of stroke in patients with atrial fibrillation? results from a multicenter study. *J. Am. Coll. Cardiol*, 60(6):531–538, 2012.

[13] Pablo Martinez-Legazpi, Lorenzo Rossini, Candelas Pérez del Villar, Yolanda Benito, Carolina Devesa-Cordero, Raquel Yotti, Antonia Delgado-Montero, Ana Gonzalez-Mansilla, Andrew M Kahn, Francisco Fernandez-Avilés, et al. Stasis mapping using ultrasound: a prospective study in acute myocardial infarction. *JACC Cardiovasc. Imaging*, 11(3):514–515, 2018.

[14] Viorel Mihalef, Razvan Ioan Ionasec, Puneet Sharma, Bogdan Georgescu, Ingmar Voigt, Michael Suehling, and Dorin Comaniciu. Patient-specific modelling of whole heart anatomy, dynamics and haemodynamics from four-dimensional cardiac ct images. *Interface Focus*, 1(3):286–296, 2011.

[15] Christophe Chnafa, Simon Mendez, and Franck Nicoud. Image-based large-eddy simulation in a realistic left heart. *Comput Fluids*, 94:173–187, 2014.

[16] Vijay Vedula. *Image based computational modeling of intracardiac flows.* PhD thesis, Johns Hopkins University, 2015.

[17] Vijay Vedula, Richard George, Laurent Younes, and Rajat Mittal. Hemodynamics in the left atrium and its effect on ventricular flow patterns. *J Biomech Eng*, 137(11), 2015.

[18] Nikoo R Saber, AD Gosman, Nigel B Wood, Philip J Kilner, Clare L Charrier, and David N Firmin. Computational flow modeling of the left ventricle based on in vivo mri data: initial experience. *Ann Biomed Eng*, 29(4):275–283, 2001.

[19] Nikoo R Saber, Nigel B Wood, AD Gosman, Robert D Merrifield, Guang-Zhong Yang, Clare L Charrier, Peter D Gatehouse, and David N Firmin. Progress towards patient-specific computational flow modeling of the left heart via combination of magnetic resonance imaging with computational fluid dynamics. *Ann Biomed Eng*, 31(1):42–52, 2003.

[20] Q Long, R Merrifield, XY Xu, DN Firmin, et al. The influence of inflow boundary conditions on intra left ventricle flow predictions. *J Biomech Eng*, 125(6):922–927, 2003.

[21] Q Long, R Merrifield, XY Xu, P Kilner, DN Firmin, and GZ Yang. Subject-specific computational simulation of left ventricular flow based on magnetic resonance imaging. *Proc Inst Mech Eng H*, 222(4):475–485, 2008.

[22] Torsten Schenkel, Mauro Malve, Michael Reik, Michael Markl, Bernd Jung, and Herbert Oertel. Mri-based cfd analysis of flow in a human left ventricle: methodology and application to a healthy heart. *Ann Biomed Eng*, 37(3):503–515, 2009.

[23] Trung Bao Le and Fotis Sotiropoulos. On the three-dimensional vortical structure of early diastolic flow in a patient-specific left ventricle. *Eur. J. Mech. B Fluids*, 35:20–24, 2012.

[24] Jung Hee Seo, Thura Abd, Richard T George, and Rajat Mittal. A coupled chemo-fluidic computational model for thrombogenesis in infarcted left ventricles. *Am. J. Physiol. Heart Circ*, 310(11):H1567–H1582, 2016.

[25] Anna Tagliabue, Luca Dedè, and Alfio Quarteroni. Complex blood flow patterns in an idealized left ventricle: A numerical study. *Chaos*, 27(9):093939, 2017.

[26] MD De Tullio, J Nam, G Pascazio, E Balaras, and Roberto Verzicco. Computational prediction of mechanical hemolysis in aortic valved prostheses. *Eur. J. Mech. B Fluids*, 35:47–53, 2012.

[27] F De Vita, MD De Tullio, and R Verzicco. Numerical simulation of the non-newtonian blood flow through a mechanical aortic valve. *Theor Comput Fluid Dyn*, 30(1-2):129–138, 2016.

[28] Jonas Lantz, Lilian Henriksson, Anders Persson, Matts Karlsson, and Tino Ebbers. Patient-specific simulation of cardiac blood flow from high-resolution computed tomography. *J Biomech Eng*, 138(12), 2016.

[29] Jonas Lantz, Vikas Gupta, Lilian Henriksson, Matts Karlsson, Anders Persson, Carl-Johan Carlhäll, and Tino Ebbers. Impact of pulmonary venous inflow on cardiac flow simulations: comparison with in vivo 4d flow mri. *Ann Biomed Eng*, 47(2):413–424, 2019.

[30] Ryo Koizumi, Kenichi Funamoto, Toshiyuki Hayase, Yusuke Kanke, Muneichi Shibata, Yasuyuki Shiraishi, and Tomoyuki Yambe. Numerical analysis of hemodynamic changes in the left atrium due to atrial fibrillation. *J. Biomech.*, 48(3):472–478, 2015.

[31] Tomohiro Otani, Abdullah Al-Issa, Amir Pourmorteza, Elliot R McVeigh, Shigeo Wada, and Hiroshi Ashikaga. A computational framework for personalized blood flow analysis in the human left atrium. *Ann Biomed Eng*, 44(11):3284–3294, 2016.

[32] Guadalupe García-Isla, Andy Luis Olivares, Etelvino Silva, Marta Nuñez-Garcia, Constantine Butakoff, Damian Sanchez-Quintana, Hernán G. Morales, Xavier Freixa, Jérôme Noailly, Tom De Potter, et al. Sensitivity analysis of geometrical parameters to study haemodynamics and thrombus formation in the left atrial appendage. *Int J Numer Method Biomed Eng*, 34(8):e3100, 2018.

[33] Giorgia Maria Bosi, Andrew Cook, Rajan Rai, Leon J Menezes, Silvia Schievano, Ryo Torii, and Gaetano Burriesci Burriesci. Computational fluid dynamic analysis of the left atrial appendage to predict thrombosis risk. *Front Cardiovasc Med*, 5:34, 2018.

[34] Alessandro Masci, Lorenzo Barone, Luca Dedè, Marco Fedele, Corrado Tomasi, Alfio Quarteroni, and Cristiana Corsi. The impact of left atrium appendage morphology on stroke risk assessment in atrial fibrillation: a computational fluid dynamics study. *Front Physiol*, 9:1938, 2019.

[35] Manuel García-Villalba, Lorenzo Rossini, Alejandro Gonzalo, Davis Vigneault, Pablo Martinez-Legazpi, Eduardo Durán, Oscar Flores, Javier Bermejo, Elliot McVeigh, Andrew M Kahn, et al. Demonstration of patient-specific simulations to assess left atrial appendage thrombogenesis risk. *Front Physiol*, 12, 2021.

[36] Shu Chien, Shunichi Usami, Robert J Dellenback, Magnus I Gregersen, Luddo B Nanninga, and M Mason Guest. Blood viscosity: influence of erythrocyte aggregation. *Science*, 157(3790):829–831, 1967.

[37] Amirhossein Arzani. Accounting for residence-time in blood rheology models: do we really need non-newtonian blood flow modelling in large arteries? *J R Soc Interface*, 15(146):20180486, 2018.

[38] Jonas Lantz, Vikas Gupta, Lilian Henriksson, Matts Karlsson, Anders Persson, Carl-Johan Carlhäll, and Tino Ebbers. Intracardiac flow at 4d ct: comparison with 4d flow mri. *Radiology*, 289(1):51–58, 2018.

[39] Alvaro Merino, Paul Hauptman, Lina Badimon, Juan Jose Badimon, Marc Cohen, Valentin Fuster, and Martin Goldman. Echocardiographic "smoke" is produced by an interaction of erythrocytes and plasma proteins modulated by shear forces. *J. Am. Coll. Cardiol*, 20(7):1661–1668, 1992.

[40] Ian W Black. Spontaneous echo contrast: where there's smoke there's fire. *Echocardiography*, 17(4):373–382, 2000.

[41] Paul A Yushkevich, Joseph Piven, Heather Cody Hazlett, Rachel Gimpel Smith, Sean Ho, James C Gee, and Guido Gerig. User-guided 3d active contour segmentation of anatomical structures: significantly improved efficiency and reliability. *Neuroimage*, 31(3):1116–1128, 2006.

[42] Qianqian Fang and David A Boas. Tetrahedral mesh generation from volumetric binary and grayscale images. In *2009 IEEE International Symposium on Biomedical Imaging: From Nano to Macro*, pages 1142–1145, 2009.

[43] Andriy Myronenko and Xubo Song. Point set registration: Coherent point drift. *IEEE PAMI*, 32(12):2262–2275, 2010.

[44] M. Moriche. *A numerical study on the aerodynamic forces and the wake stability of flapping flight at low Reynolds number*. PhD thesis, Univ. Carlos III Madrid, 2017.

[45] M. Moriche, O. Flores, and M. García-Villalba. On the aerodynamic forces on heaving and pitching airfoils at low Reynolds number. *J. Fluid Mech.*, 828:395–423, 2017.

[46] O Flores, L Rossini, A Gonzalo, D Vigneault, J Bermejo, AM Kahn, E McVeigh, M García-Villalba, and JC del Álamo. Evaluation of blood stasis in the left atrium using patient-specific direct numerical simulations. In *ERCOFTAC Workshop Direct and Large Eddy Simulation XII*, pages 485–490. Springer, 2019.

[47] Giovanni P Galdi, Rolf Rannacher, Anne M Robertson, and Stefan Turek. Hemodynamical flows. *Delhi Book Store*, 2008.

[48] Lorenzo Rossini, Pablo Martinez-Legazpi, Vi Vu, Leticia Fernandez-Friera, Candelas Pérez Del Villar, Sara Rodriguez-Lopez, Yolanda Benito, Maria-Guadalupe Borja, David Pastor-Escuredo, Raquel Yotti, et al. A clinical method for mapping and quantifying blood stasis in the left ventricle. *J. Biomech*, 49(11):2152–2161, 2016.

[49] Chi-Wang Shu. Essentially non-oscillatory and weighted essentially non-oscillatory schemes for hyperbolic conservation laws. In *Advanced numerical approximation of nonlinear hyperbolic equations*, pages 325–432. Springer, 1998.

[50] M. Uhlmann. An immersed boundary method with direct forcing for the simulation of particulate flows. *J. Comput. Phys.*, 209(2):448–476, 2005.

[51] E Duran, M Garcia-Villalba, L Rossini, A Gonzalo, D Vigneault, P Martinez-Legazpi, J Bermejo, E McVeigh, AM Kahn, JC Del Alamo, et al. Effect of pulmonary vein inflow on patient-specific cfd prediction of left atrial blood stasis. *Bull. Am. Phys. Soc*, 2020.

[52] Armin Leuprecht and Karl Perktold. Computer simulation of non-newtonian effects on blood flow in large arteries. *Comput Methods Biomech Biomed Engin*, 4(2):149–163, 2001.

[53] Mohammed G Al-Azawy, A Turan, and Alistair Revell. Investigating the impact of non-newtonian blood models within a heart pump. *Int J Numer Method Biomed Eng*, 33(1):e02780, 2017.

[54] Shu Chien, SHUNICHI Usami, Harry M Taylor, John L Lundberg, and Magnus I Gregersen. Effects of hematocrit and plasma proteins on human blood rheology at low shear rates. *J. Appl. Physiol*, 21(1):81–87, 1966.

[55] Brian Devine. *Mean blood hematocrit of adults: United States, 1960-1962*. Number 19-24. US Department of Health, Education, and Welfare, Public Health Service, 1967.

[56] Henny H Billett. Hemoglobin and hematocrit. *Clinical Methods: The History, Physical, and Laboratory Examinations. 3rd edition*, 1990.

[57] CR Huang and W Fabisiak. Thixotropic parameters of whole human blood. *Thromb. Res*, 8:1–8, 1976.

[58] H Schmid-Schönbein, E Volger, and HJ Klose. Microrheology and light transmission of blood. *Pflügers Archiv*, 333(2):140–155, 1972.

[59] MJ Davies and Ariela Pomerance. Pathology of atrial fibrillation in man. *Br. Heart J*, 34(5):520, 1972.

[60] Joseph L Blackshear and John A Odell. Appendage obliteration to reduce stroke in cardiac surgical patients with atrial fibrillation. *Ann. Thorac. Surg*, 61(2):755–759, 1996.

[61] Diane Fatkin, Raymond P Kelly, and Michael P Feneley. Relations between left atrial appendage blood flow velocity, spontaneous echocardiographic contrast and thromboembolic risk in vivo. *J. Am. Coll. Cardiol*, 23(4):961–969, 1994.

[62] UDIPI R Shettigar, MARTIN Dropmann, PAUL E Christian, and WILLEM J Kolff. Residence time distributions in artificial ventricles. *ASAIO Trans*, 35(3):708–712, 1989.

[63] Sahar Hendabadi, Javier Bermejo, Yolanda Benito, Raquel Yotti, Francisco Fernández-Avilés, Juan C Del Álamo, and Shawn C Shadden. Topology of blood transport in the human left ventricle by novel processing of doppler echocardiography. *Ann Biomed Eng*, 41(12):2603–2616, 2013.

[64] Jonatan Eriksson, Carl Johan Carlhäll, Petter Dyverfeldt, Jan Engvall, Ann F Bolger, and Tino Ebbers. Semi-automatic quantification of 4d left ventricular blood flow. *J Cardiovasc Magn Reson*, 12(1):1–10, 2010.

[65] Antonia Delgado-Montero, Pablo Martinez-Legazpi, M Mar Desco, Daniel Rodríguez-Pérez, Fernando Díaz-Otero, Lorenzo Rossini, Candelas Pérez Del Villar, Elena Rodríguez-González, Christian Chazo, Yolanda Benito, et al. Blood stasis imaging predicts cerebral microembolism during acute myocardial infarction. *J Am Soc Echocardiogr*, 33(3):389–398, 2020.

[66] Jung Hee Seo and Rajat Mittal. Effect of diastolic flow patterns on the function of the left ventricle. *Phys. Fluids*, 25(11):110801, 2013.

[67] Soroosh Sanatkhani, Sotirios Nedios, Prahlad G Menon, Andreas Bollmann, Gerhard Hindricks, and Sanjeev G Shroff. Subject-specific calculation of left atrial appendage blood-borne particle residence time distribution in atrial fibrillation. *Front Physiol*, 12, 2021.

[68] Danila Vella, Alessandra Monteleone, Giulio Musotto, Giorgia Maria Bosi, and Gaetano Burriesci. Effect of the alterations in contractility and morphology produced by atrial fibrillation on the thrombosis potential of the left atrial appendage. *Front. Bioeng. Biotechnol*, 9:147, 2021.

[69] Ian W Black, Colin N Chesterman, Andrew P Hopkins, Lincoln CL Lee, Beng H Chong, and Warren F Walsh. Hematologic correlates of left atrial spontaneous echo contrast and thromboembolism in nonvalvular atrial fibrillation. *J. Am. Coll. Cardiol*, 21(2):451–457, 1993.

[70] Andreas Mügge, Henning Kühn, Peter Nikutta, Jochen Grote, J Antonio G. Lopez, and Werner G Daniel. Assessment of left atrial appendage function by biplane transesophageal echocardiography in patients with nonrheumatic atrial fibrillation: identification of a subgroup of patients at increased embolic risk. *J. Am. Coll. Cardiol*, 23(3):599–607, 1994.

[71] Massimo Pozzoli, Oreste Febo, Adam Torbicki, Roberto Tramarin, Giuseppe Calsamiglia, Franco Cobelli, Giuseppe Specchia, and Joseph RTC Roelandt. Left atrial appendage dysfunction: a cause of thrombosis? evidence by transesophageal echocardiography-doppler studies. *J Am Soc Echocardiogr*, 4(5):435–441, 1991.

[72] Patrick MJ Verhorst, Otto Kamp, Cees A Visser, and Freek WA Verheugt. Left atrial appendage flow velocity assessment using transesophageal echocardiography in nonrheumatic atrial fibrillation and systemic embolism. *Am. J. Cardiol*, 71(2):192–196, 1993.

[73] Hisanori SHINOHARA, Nobuo FUKUDA, Takeshi SOEKI, Naoki TAKEICHI, Yasuko Yui, Yoshiyuki TAMURA, and Takashi OKI. Relationship between flow dynamics in the left atrium and hemostatic abnormalities in patients with nonvalvular atrial fibrillation. *Jpn Heart J*, 39(6):721–730, 1998.

[74] Martin E Goldman, Lesly A Pearce, Robert G Hart, Miguel Zabalgoitia, Richard W Asinger, Robert Safford, Jonathan L Halperin, Stroke Prevention in Atrial Fibrillation Investigators, et al. Pathophysiologic correlates of thromboembolism in nonvalvular atrial fibrillation: I. reduced flow velocity in the left atrial appendage (the stroke prevention in atrial fibrillation [spaf-iii] study). *J Am Soc Echocardiogr*, 12(12):1080–1087, 1999.

[75] Yan Wang, Yonghui Qiao, Yankai Mao, Chenyang Jiang, Jianren Fan, and Kun Luo. Numerical prediction of thrombosis risk in left atrium under atrial fibrillation. *Math Biosci Eng*, 17(3):2348–2360, 2020.

[76] Jacopo Biasetti, T Christian Gasser, Martin Auer, Ulf Hedin, and Fausto Labruto. Hemodynamics of the normal aorta compared to fusiform and saccular abdominal aortic aneurysms with emphasis on a potential thrombus formation mechanism. *Ann Biomed Eng*, 38(2):380–390, 2010.

[77] Siamak N Doost, Liang Zhong, Boyang Su, and Yosry S Morsi. The numerical analysis of non-newtonian blood flow in human patient-specific left ventricle. *Comput Methods Programs Biomed*, 127:232–247, 2016.

[78] H Schmid-Schönbein, JV Gosen, L Heinich, HJ Klose, and E Volger. A counter-rotating "rheoscope chamber" for the study of the microrheology of blood cell aggregation by microscopic observation and microphotometry. *Microvasc. Res*, 6(3):366–376, 1973.

[79] Nadia Antonova, Pavel Riha, and Ivan Ivanov. Time dependent variation of human blood conductivity as a method for an estimation of rbc aggregation. *Clin. Hemorheol. Microcirc*, 39(1–4):69–78, 2008.

[80] Ga-Young Suh, Andrea S Les, Adam S Tenforde, Shawn C Shadden, Ryan L Spilker, Janice J Yeung, Christopher P Cheng, Robert J Herfkens, Ronald L Dalman, and Charles A Taylor. Quantification of particle residence time in abdominal aortic aneurysms using magnetic resonance imaging and computational fluid dynamics. *Ann Biomed Eng*, 39(2):864–883, 2011.

[81] Ramon Castello, Anthony C Pearson, Leonard Fagan, and Arthur J Labovitz. Spontaneous echocardiographic contrast in the descending aorta. *Am. Heart J*, 120(4):915–919, 1990.

[82] Xiaodong Zhou, Ruiyu Shi, Gaojun Wu, Qianli Zhu, Changzuan Zhou, Liangguo Wang, Chenglong Xue, Yuanyuan Jiang, Xueli Cai, Weijian Huang, et al. The prevalence, predictors, and outcomes of spontaneous echocardiographic contrast or left ventricular thrombus in patients with hfref. *ESC Heart Fail*, 8(2):1284–1294, 2021.

[83] Alessandra Riva, Francesco Sturla, Alessandro Caimi, Silvia Pica, Daniel Giese, Paolo Milani, Giovanni Palladini, Massimo Lombardi, Alberto Redaelli, and Emiliano Votta. 4d flow evaluation of blood non-newtonian behavior in left ventricle flow analysis. *J. Biomech.*, 119:110308, 2021.

[84] Yolanda Benito, Pablo Martinez-Legazpi, Lorenzo Rossini, Candelas Perez del Villar, Raquel Yotti, Yolanda Martin Peinador, Daniel Rodriguez-Perez, M Desco, Constancio Medrano, Jose Carlos Antoranz, et al. Age-dependence of flow homeostasis in the left ventricle. *Front Physiol*, 10:485, 2019.

[85] Hideo Tohgi, HIROSHI Yamanouchi, MOTOTAKA Murakami, and MASAKUNI Kameyama. Importance of the hematocrit as a risk factor in cerebral infarction. *Stroke*, 9(4):369–374, 1978.

[86] Renling Yang, Anxin Wang, Li Ma, Zhaoping Su, Shuohua Chen, Yilong Wang, Shouling Wu, and Chen Wang. Hematocrit and the incidence of stroke: a prospective, population-based cohort study. *Ther Clin Risk Manag*, 14:2081, 2018.

[87] Vivek Vasudevan, Adriel Jia Jun Low, Sarayu Parimal Annamalai, Smita Sampath, Kian Keong Poh, Teresa Totman, Muhammad Mazlan, Grace Croft, A Mark Richards, Dominique PV de Kleijn, et al. Flow dynamics and energy efficiency of flow in the left ventricle during myocardial infarction. *Biomech. Model. Mechanobiol*, 16(5):1503–1517, 2017.

[88] Lorenzo Rossini, Pablo Martinez-Legazpi, Yolanda Benito, Candelas Pérez Del Villar, Ana Gonzalez-Mansilla, Alicia Barrio, Maria-Guadalupe Borja, Raquel Yotti, Andrew M Kahn, Shawn C Shadden, et al. Clinical assessment of intraventricular blood transport in patients undergoing cardiac resynchronization therapy. *Meccanica*, 52(3):563–576, 2017.

[89] Alessandro Masci, Martino Alessandrini, Davide Forti, Filippo Menghini, Luca Dedé, Corrado Tomasi, Alfio Quarteroni, and Cristiana Corsi. A proof of concept for computational fluid dynamic analysis of the left atrium in atrial fibrillation on a patient-specific basis. *J Biomech Eng*, 142(1), 2020.

[90] John Ross Jr, Eugene Braunwald, and Andrew G Morrow. Transseptal left atrial puncture: new technique for the measurement of left atrial pressure in man. *Am. J. Cardiol*, 3(5):653–655, 1959.

[91] C Stefanadis, J Dernellis, and P Toutouzas. A clinical appraisal of left atrial function. *Eur. Heart J*, 22(1):22–36, 2001.

[92] Paul S Pagel, Franz Kehl, Meir Gare, Douglas A Hettrick, Judy R Kersten, and David C Warltier. Mechanical function of the left atrium: new insights based on analysis of pressure–volume relations and doppler echocardiography. *Anesthesiology*.